Defense Threat Reduction Agency
8725 John J. Kingman Road, MS 6201
Fort Belvoir, VA 22060-6201

High Power Electromagnetic (HPEM) Threat Analysis

TECHNICAL REPORT

April 2008

Edl Schamiloglu et al.

Prepared by:
U. of New Mexico
Department of Electrical and Computer
Engineering
Albuquerque, NM 87131-0001

20080811 039

REPORT DOCUMENTATION PAGE

Public reporting burden for this collection of information is estimated to average 1 hour per response, including the time for reviewing instructions, searching existing data sources, gathering and maintaining the data needed, and completing and reviewing this collection of information. Send comments regarding this burden estimate or any other aspect of this collection of information, including suggestions for reducing this burden to Department of Defense, Washington Headquarters Services, Directorate for Information Operations and Reports (0704-0188), 1215 Jefferson Davis Highway, Suite 1204, Arlington, VA 22202-4302. Respondents should be aware that notwithstanding any other provision of law, no person shall be subject to any penalty for failing to comply with a collection of information if it does not display a currently valid OMB control number. **PLEASE DO NOT RETURN YOUR FORM TO THE ABOVE ADDRESS.**

1. REPORT DATE *(DD-MM-YYYY)*	2. REPORT TYPE	3. DATES COVERED *(From - To)*
		82004-06192006

4. TITLE AND SUBTITLE

High Power Electromagnetic (HPEM) Threat Analysis

5a. CONTRACT NUMBER
DTRA 01-03-D-0009/D.O. 4

5b. GRANT NUMBER

5c. PROGRAM ELEMENT NUMBER
468D

6. AUTHOR(S)

Edl Schamiloglu, Christos Christodoulou, John Gaudet, Jerald Buchenauer,

Paul Cravens, Michael Lambrecht, Constantina Lambrinos,

Russell Jedlicka, Bruce Blevins, Fred Tesche, and Dave Giri.

5d. PROJECT NUMBER
BD

5e. TASK NUMBER
AB

5f. WORK UNIT NUMBER
DH10698

7. PERFORMING ORGANIZATION NAME(S) AND ADDRESS(ES)

University of New Mexico, Department of Electrical and Computer Engineering, Albuquerque, NM 87131-0001; New Mexico State University, Department of Electrical and Computer Engineering and Physical Sciences Laboratory, PSL WSMR Operations Bldg 1815, White Sands Missile Range, NM 88002; Electromagnetics Consultant, 1519 Miller Mountain Rd., Saluda, NC 28773; Pro-Tech 11-C Orchard Court, Alamo, CA 94507-1541

8. PERFORMING ORGANIZATION REPORT NUMBER

9. SPONSORING / MONITORING AGENCY NAME(S) AND ADDRESS(ES)

Defense Threat Reduction Agency
8725 John J. Kingman Road, MS 6201
Fort Belvoir, VA 22060-6201

10. SPONSOR/MONITOR'S ACRONYM(S)
DTRA-TR-06-28

11. SPONSOR/MONITOR'S REPORT NUMBER(S)

12. DISTRIBUTION / AVAILABILITY STATEMENT

Distribution Statement A - Approved for public release; distribution is unlimited.

13. SUPPLEMENTARY NOTES

14. ABSTRACT

We live in a modern world supported by large, complex networks. Examples range from financial markets to communication and transportation systems, and all manners of networks pertinent to the mission of the DoD. In many realistic situations the flow of physical quantities in the network, as characterized by the loads on nodes, is important. In today's modern world where sensitive electronics are omnipresent, High Power Eelectromagnetic (HPEM) threats represent an emerging threat that could disrupt nodes, thereby interrupting the functionality of the complex network. This final report describes an overarching paradigm for modeling such threats. Suggestions for future research, based on deficiencies found in existing approaches, comprise the key conclusions of this study.

15. SUBJECT TERMS

High Power Microwaves	Topological Analysis
High Power Electromagnetics	Statistical Electromagnetics

16. SECURITY CLASSIFICATION OF:			17. LIMITATION OF ABSTRACT	18. NUMBER OF PAGES	19a. NAME OF RESPONSIBLE PERSON
a. REPORT U	b. ABSTRACT U	c. THIS PAGE U	SAR		19b. TELEPHONE NUMBER *(include area code)*

CONVERSION TABLE

Conversion Factors for U.S. Customary to metric (SI) units of measurement.

MULTIPLY ————————————→ BY ————————————→ TO GET

TO GET ←———————————— BY ←———————————— DIVIDE

angstrom	1.000 000 x E -10	meters (m)
atmosphere (normal)	1.013 25 x E +2	kilo pascal (kPa)
bar	1.000 000 x E +2	kilo pascal (kPa)
barn	1.000 000 x E -28	meter^2 (m^2)
British thermal unit (thermochemical)	1.054 350 x E +3	joule (J)
calorie (thermochemical)	4.184 000	joule (J)
cal (thermochemical/cm^2)	4.184 000 x E -2	mega joule/m^2 (MJ/m^2)
curie	3.700 000 x E +1	*giga bacquerel (GBq)
degree (angle)	1.745 329 x E -2	radian (rad)
degree Fahrenheit	$t_k = (t°f + 459.67)/1.8$	degree kelvin (K)
electron volt	1.602 19 x E -19	joule (J)
erg	1.000 000 x E -7	joule (J)
erg/second	1.000 000 x E -7	watt (W)
foot	3.048 000 x E -1	meter (m)
foot-pound-force	1.355 818	joule (J)
gallon (U.S. liquid)	3.785 412 x E -3	meter^3 (m^3)
inch	2.540 000 x E -2	meter (m)
jerk	1.000 000 x E +9	joule (J)
joule/kilogram (J/kg) radiation dose absorbed	1.000 000	Gray (Gy)
kilotons	4.183	terajoules
kip (1000 lbf)	4.448 222 x E +3	newton (N)
kip/inch^2 (ksi)	6.894 757 x E +3	kilo pascal (kPa)
ktap	1.000 000 x E +2	newton-second/m^2 (N-s/m^2)
micron	1.000 000 x E -6	meter (m)
mil	2.540 000 x E -5	meter (m)
mile (international)	1.609 344 x E +3	meter (m)
ounce	2.834 952 x E -2	kilogram (kg)
pound-force (lbs avoirdupois)	4.448 222	newton (N)
pound-force inch	1.129 848 x E -1	newton-meter (N-m)
pound-force/inch	1.751 268 x E +2	newton/meter (N/m)
pound-force/foot^2	4.788 026 x E -2	kilo pascal (kPa)
pound-force/inch^2 (psi)	6.894 757	kilo pascal (kPa)
pound-mass (lbm avoirdupois)	4.535 924 x E -1	kilogram (kg)
pound-mass-foot^2 (moment of inertia)	4.214 011 x E -2	kilogram-meter^2 (kg-m^2)
pound-mass/foot^3	1.601 846 x E +1	kilogram-meter^3 (kg/m^3)
rad (radiation dose absorbed)	1.000 000 x E -2	**Gray (Gy)
roentgen	2.579 760 x E -4	coulomb/kilogram (C/kg)
shake	1.000 000 x E -8	second (s)
slug	1.459 390 x E +1	kilogram (kg)
torr (mm Hg, 0° C)	1.333 22 x E -1	kilo pascal (kPa)

*The bacquerel (Bq) is the SI unit of radioactivity; 1 Bq = 1 event/s.
**The Gray (GY) is the SI unit of absorbed radiation.

TABLE OF CONTENTS

Figures

SECTION 1

INTRODUCTION

We live in a modern world supported by large, complex networks [1]. Examples range from financial markets to communication and transportation systems, and all manners of networks pertinent to the mission of the Department of Defense (DoD). In many realistic situations the flow of physical quantities in the network, as characterized by the loads on nodes, is important. In today's modern world where sensitive electronics are omnipresent, High Power Electromagnetic (HPEM) threats represent an emerging threat that could disrupt nodes, thereby interrupting the functionality of the complex network. (See, for example, Appendices A and B for additional information on these aspects.) This report describes an overarching paradigm for modeling such threats. Suggestions for future research, based on deficiencies found in existing approaches, comprise the key conclusions of this study.

The Defense Threat Reduction Agency (DTRA) safeguards the United States and its allies from weapons of mass destruction (chemical, biological, radiological, nuclear and high explosives) by providing capabilities to reduce, eliminate and counter the threat and mitigate its effects. This combat support agency serves as the intellectual, technical and operational leader for the DoD in the national effort to combat weapons of mass destruction. Established in 1998, this year DTRA celebrates 10 years of creative solutions through teamwork.

SECTION 2

SUMMARY OF MEASUREMENTS AND NEED FOR STATISTICAL ELECTROMAGNETICS

2.1 ROOM 118 ECE BUILDING EXPERIMENTAL SET-UP

The UNM-led team decided to perform active measurements of the EM environment in Room 118 of the ECE Building in order to better understand the sensitivity of the measurements to subtle changes in the boundary conditions of the room. This was motivated by the ambiguity in interpreting many aspects of the passive measurements previously performed at the DTRA TEAMS. The experimental set-up is shown in Figure 1.
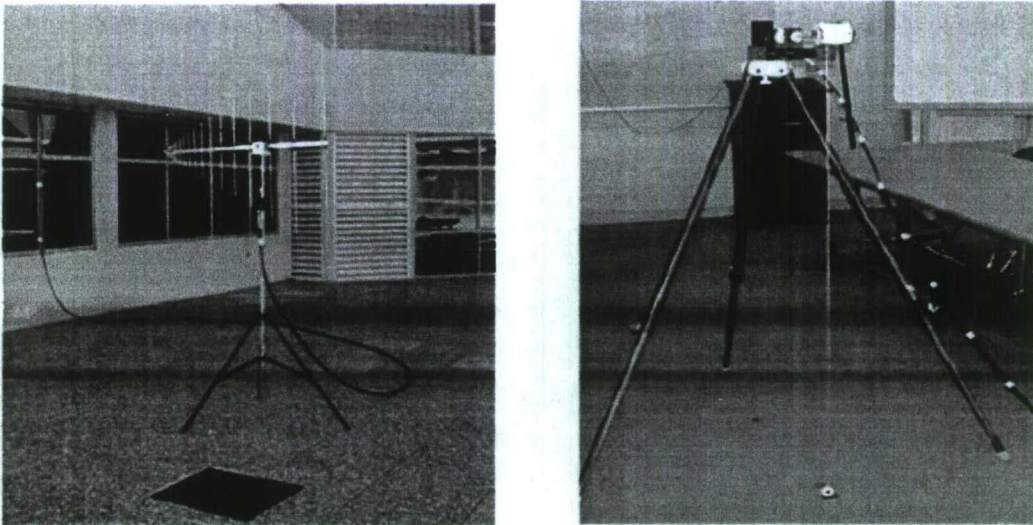
Figure 1. Set-up for experimental measurements in 118 ECE Building. Shown are the log-periodic transmitting antenna (left) and the receiving antenna (right).

There were several sets of tests performed in the room. In the first set of tests, the receiving antenna was placed at different locations in the room to determine the variation in frequency with respect to the spatial position of the receiving antenna. In the next set of tests several obstacles were arranged between the transmitting antenna and the receiving antenna. Additionally, there were variations made in the number of persons seated next to the receiving antenna, and variations in external excitations (such as the fluorescent lights overhead) to determine the effect on the incident field strength in the room. The data recorded from the sets of tests, along with graphs that were made from the measured data, are summarized in the next subsection.

2.2 ROOM 118 ECE BUILDING EXPERIMENTAL DATA

Figures 2-4 summarize some of the data that was taken in Room 118. In Figs. 2 and 3, a series of standing waves are shown which were the results of the energy radiated into Room 118 during the experiment. Figure 4 shows the relation between the B-dot receiver and D-dot receiver measurements. Resonant frequencies are also observed for selected data.

These standing waves were the result of wave energy that was coupled into the room. These standing waves are indicative of a "pumping mechanism" [2] which can be so damaging to sensitive electronics from high power microwave incident waves, as each successive wave of energy illuminates the electronics with damaging high power, and subsequent localized heating of the components.
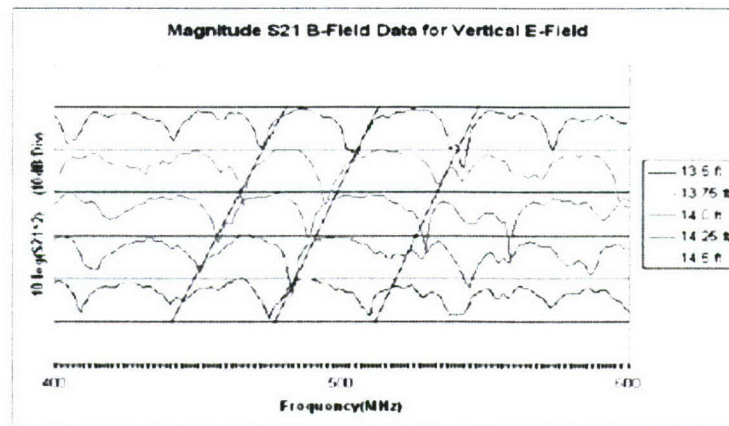
Figure 2. Standing waves (B-field data) in Room 118.
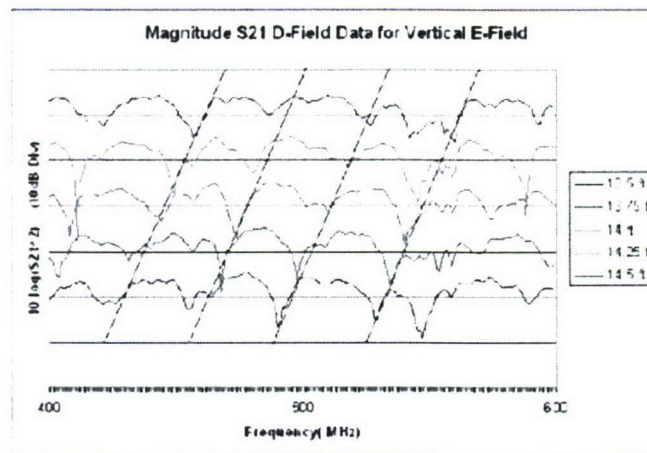
Figure 3. Standing Waves (D-Field data) in Room 118.

Comparison of B-Dot & D-Dot Data at 14 ft for Vertical E-Field
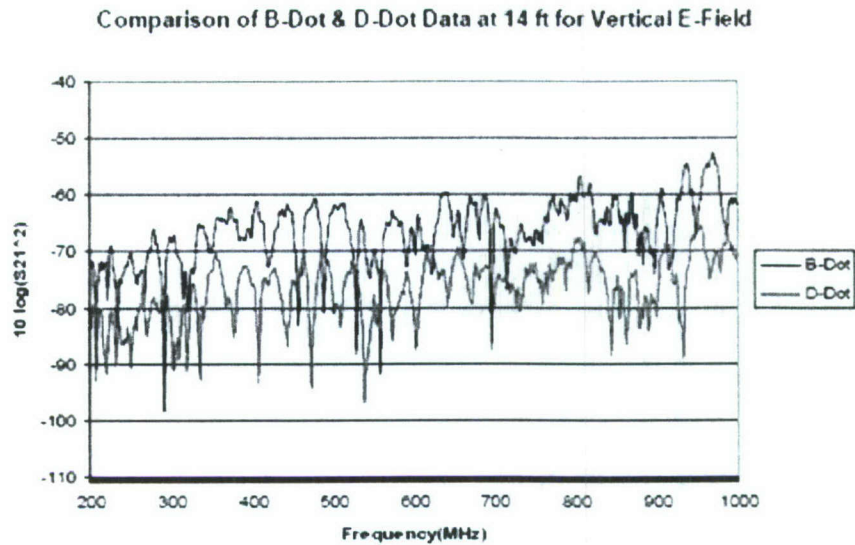
Figure 4. Comparison of B-field and D-field data.

Additional data are now presented. The preamble of each data set describes the set-up and conditions for the experiment.

Outside Log Periodic Antenna: 17 feet from the third pillar; blinds in 118 ECE Building are open

1. VERTICAL POLARIZATION

1.1 Inside B-dot Probe: 14 feet from the third pillar (initial) and moved 3.6 inches, 57.25 inches high, 117 inches from the door. Positions 1-5 below are referenced in the figures that follow.

1   13.5 inches from the third pillar
2   13.75 inches from the third pillar
3   14 inches from the third pillar
4   14.25 inches from the third pillar
5   14.5 inches from the third pillar
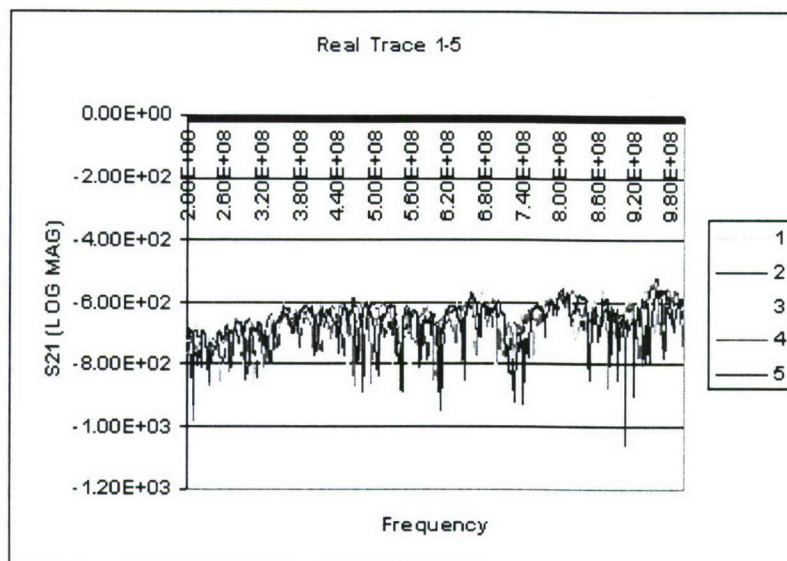
Figure 5. B-Dot probe measurements for 5 different positions inside.
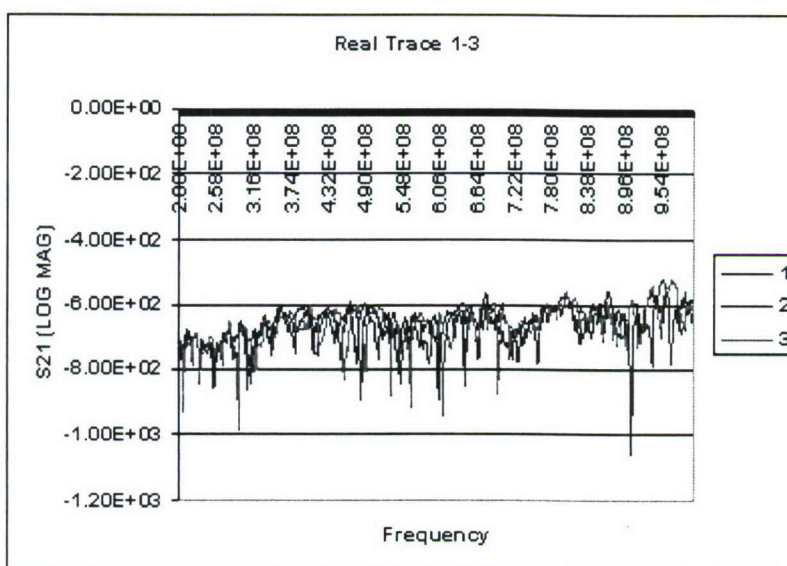
Figure 6. B-Dot probe measurements focusing on 3 of the 5 different positions inside.
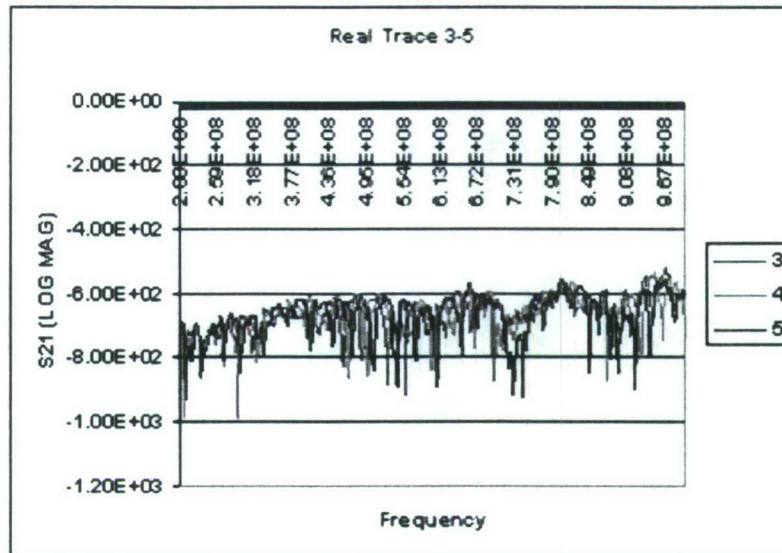
Figure 7. B-Dot probe measurements for 3 of the 5 different positions inside.

1.2. Inside D-dot Probe: 14 feet from the third pillar (initial) and moved 3.6 inches, 57.25 inches high, 117 inches from the door.

6   13.5 inches from the third pillar
7   13.75 inches from the third pillar
8   14 inches from the third pillar
9   14.25 inches from the third pillar
10   14.5 inches from the third pillar
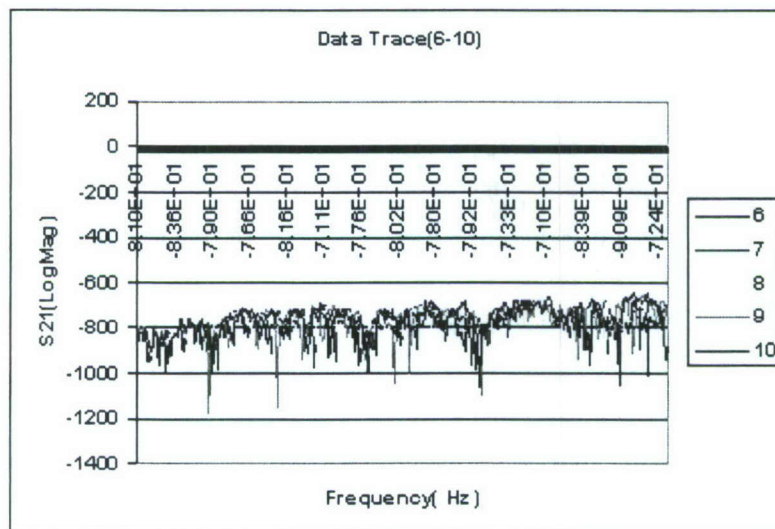
Figure 8. D-Dot probe measurements for 5 different positions inside.
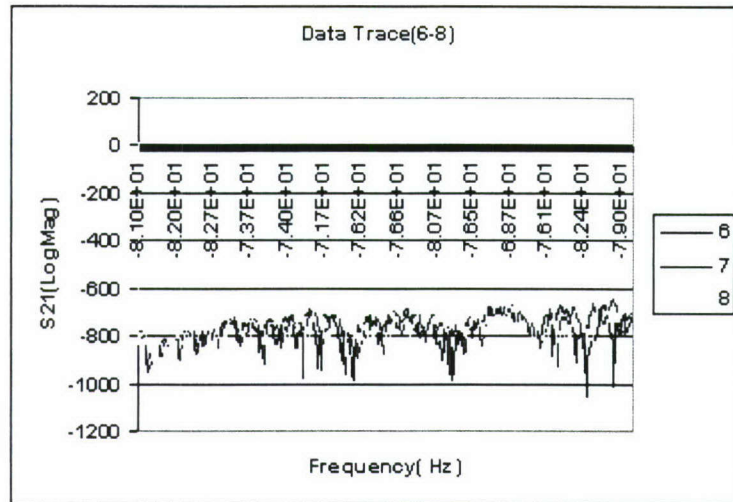
Figure 9. D-Dot probe measurements for 3 of the 5 different positions inside.
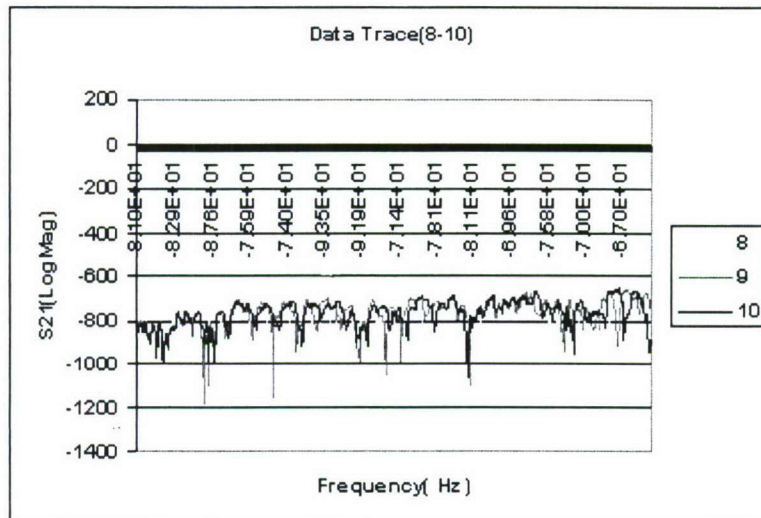
Figure 10. D-Dot probe measurements for 3 of the 5 different positions inside.

2. 14 feet from Third Pillar

Memory: blinds up but vertical
Data: blinds down, lures horizontal
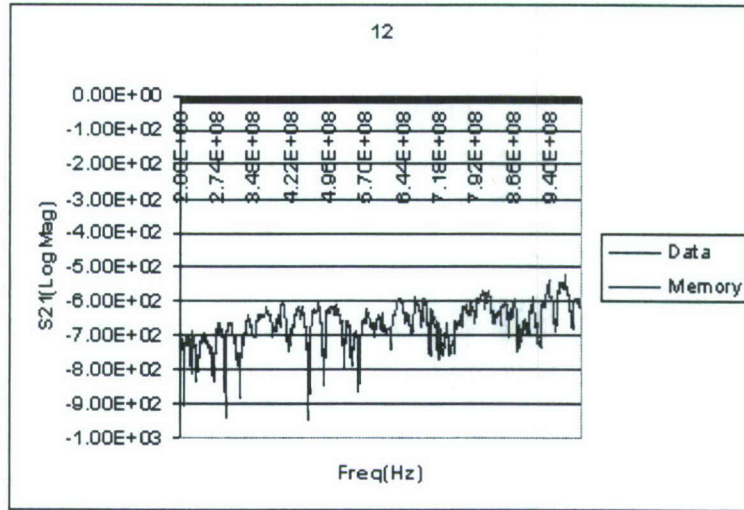
Figure 11. Comparison of effect of the blind configuration.

3. 14 feet from Third Pillar
Memory: Vertical Polarization Blinds up (open)
Data: Horizontal Polarization Blinds up (open)
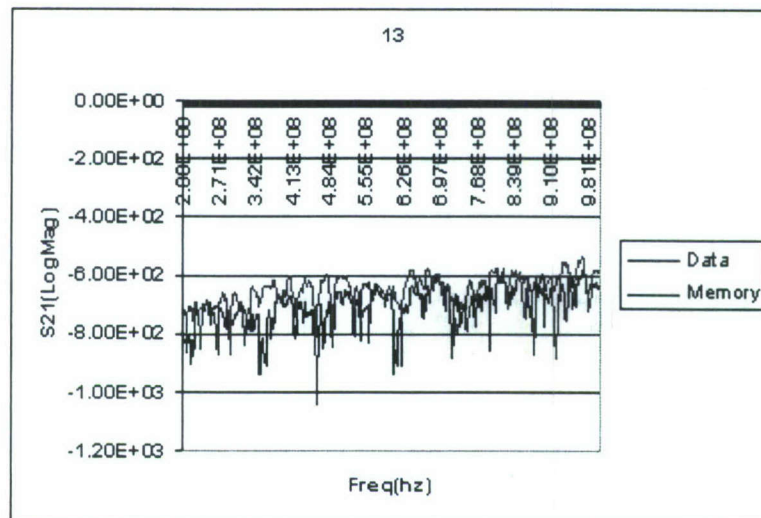
Figure 12. Comparison of effect of blind configuration.

4. 14 feet from Third Pillar

Memory: Blinds down, lures vertical
Data: Blinds open
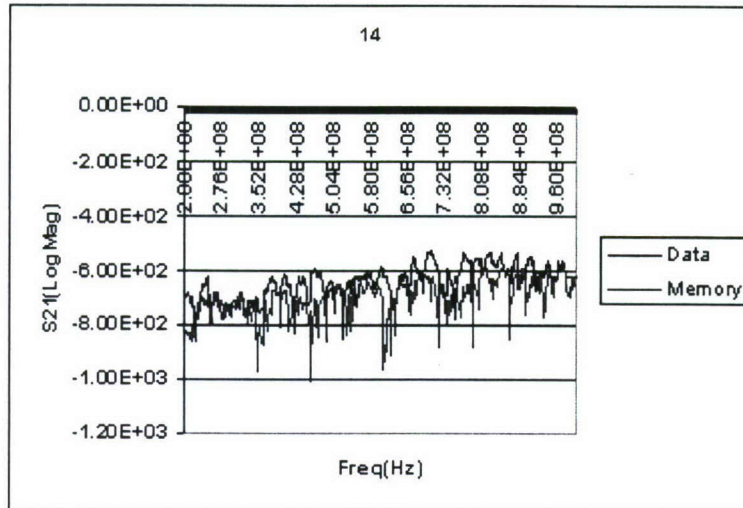
Figure 13. Comparison of effect of blind configuration.

5. Effect of file cabinet

Without file Cabinet
Saved as Memory

5.1 With file Cabinet Different Location
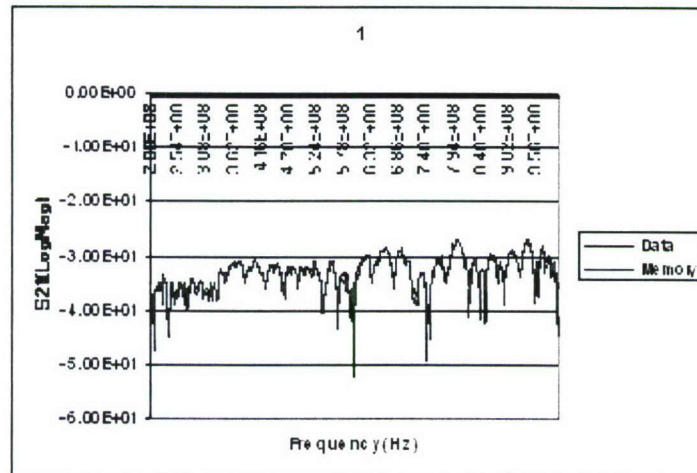
Figure 14. Effect of file cabinet in front of entrance to Room 118.
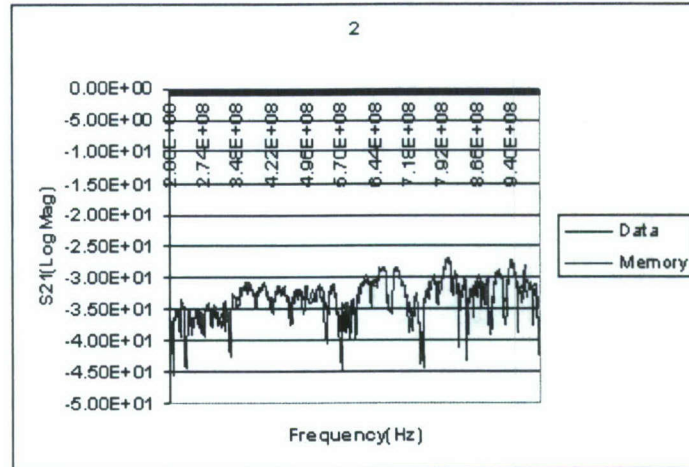
Figure 15. Effect of file cabinet in front of whiteboard in Room 118.
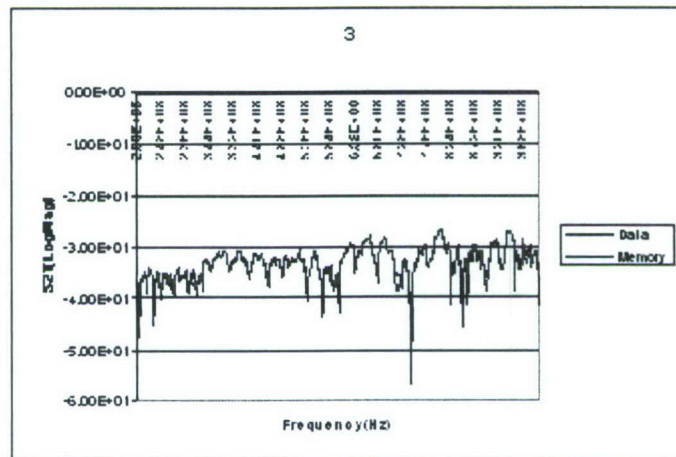
Figure 16. Effect of file cabinet across from entrance to Room 118.
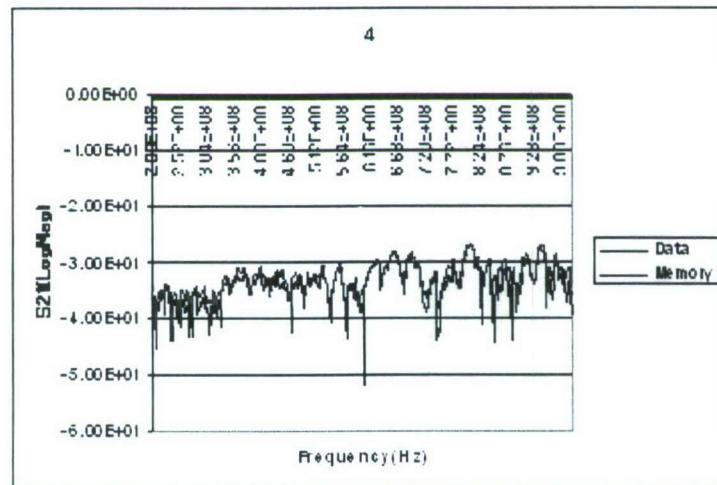
Figure 17. Effect of file cabinet in front of receiving antenna in Room 118.

5.2 Without file cabinet & time delay 134 ns

5.2.1. Sitting in front of the network analyzer& one person
data: leaning forward
memory: leaning backward
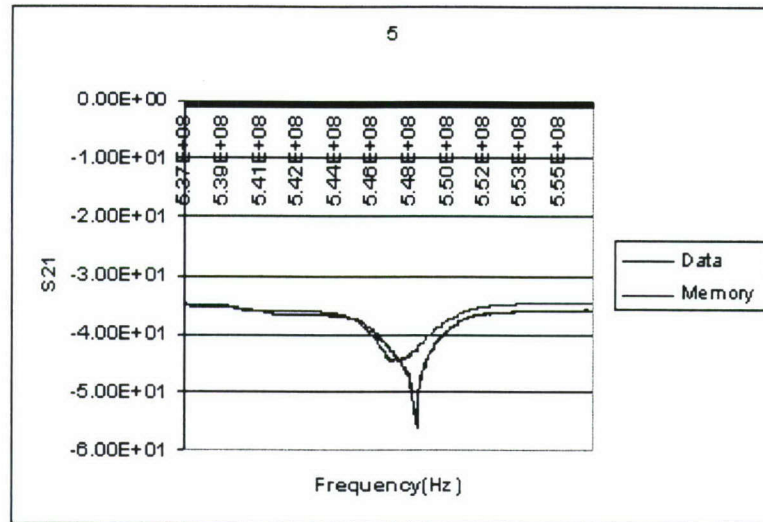
Figure 18. Effect of one person leaning forward while taking data on network analyzer.

5.2.2 Change from #5
data: two people
memory: one person
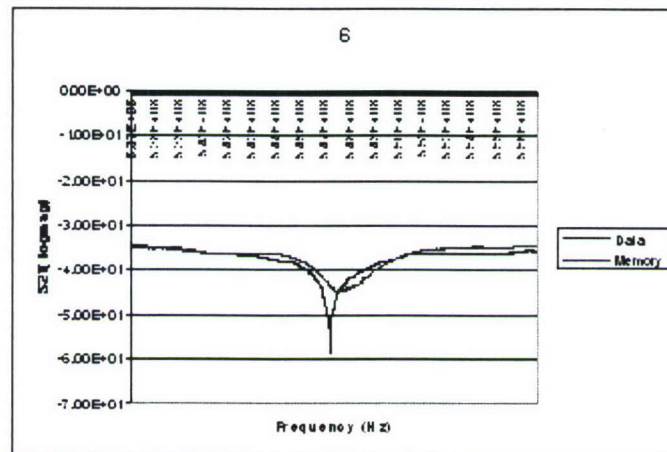
Figure 19. Effect of two people vs. one person leaning forward while taking data on network analyzer.

5.2.3. Lights on or off with one person in room
data: off
memory: on
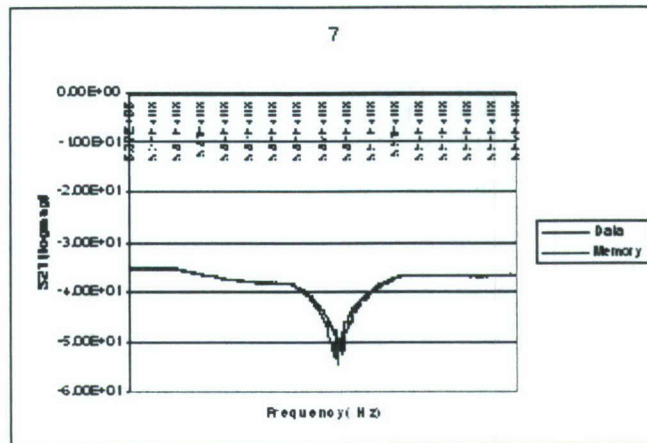
Figure 20. Effect of fluorescent ceiling lights on or off with respect to one person leaning forward while taking data on network analyzer.

5.2.4 Same as #7 Lights on or off with one person in room
data: on
memory: off
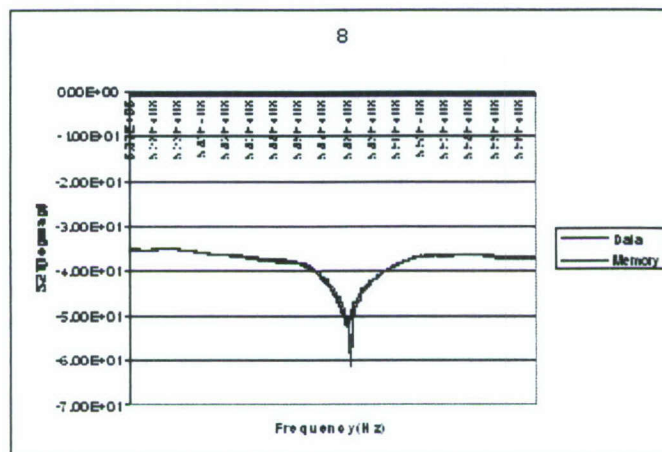
Figure 21. Effect of fluorescent ceiling lights on or off with respect to one person leaning forward while taking data on network analyzer (repeat of previous experiment).

The sensitivity of the measurements to subtle changes in the electromagnetic boundary conditions argues for a statistical approach to solving this problem. This realization ties in naturally to the recent theoretical and experimental work at the University of Maryland where researches have been pioneering a statistical electromagnetics description of chaotic cavities [3]. In this regard, Room 118 can be viewed as a chaotic cavity.

2.3 RELATIONSHIP OF EMP THREATS TO HPEM EMERGING THREATS

Although the research described in this report focused on HPEM emerging threats, there are some aspects that are in common with the nuclear EMP threats and some aspects that are quite different. Figure 22 presents a sketch of various frequency bands associated with EM threats. Note that the nuclear EMP threat occurs at a factor of 10 or lower frequency than the emerging HPEM threats. Traditional methods of circuit protection developed to counter the nuclear EMP threat will not always suffice to protect against HPEM. Lower operating voltages, smaller device sizes, and faster switching speed also make these devices more susceptible to damage from high power microwaves.
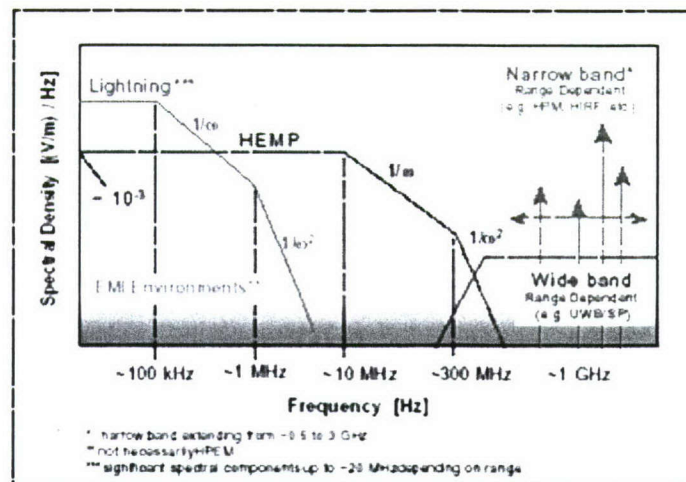
Figure 22. Various bands summarizing EM threats.

HEMP coupling characteristics

In the early 1960's, researchers proposed a theory that a high-altitude nuclear explosion could produce a nuclear electromagnetic pulse (HEMP) that would couple enough energy to electronic equipment and some electrical equipment to render the equipment useless and unavailable for critical infrastructure. Steps were taken immediately to find ways to safeguard the electronics comprising the infrastructure throughout the United States and among some western allies. Examples of these safeguards included interior rooms, metal cabinets, and enclosures to remove the equipment from physical and electromagnetic threats.

"HEMP occurs typically at high altitudes (30 – 300 km) and produces a fast rise-time, high amplitude pulse of short duration, which is followed by a lower amplitude pulse, which gradually diminishes and lasts for minutes after the initial detonation. HEMP couples to conductors including power lines, telephone lines, pipelines and conductors within buildings, down to direct interaction with electronic chips and circuits." The detonation of the nuclear device at high altitude is crucial to the generation of the HEMP. **"The radiation from a nuclear explosion ionizes the air and creates a temporally changing current system that launches the HEMP. This current system consists of two parts: 1) energetic electrons (~1-MeV) produced by Compton scattering of the γ-rays and moving radially outward, and 2) secondary**

electrons that are produced by both X-rays (photoelectric effect) and ionization of the air by the Compton electrons. At low altitudes, X-rays are easily absorbed in air and … contribute little to the currents that generate HEMP. At high altitudes (> 50 km) X-rays become important both in creating a current system that contribute to the HEMP and that creates background ionization that absorbs some of the HEMP". [4]
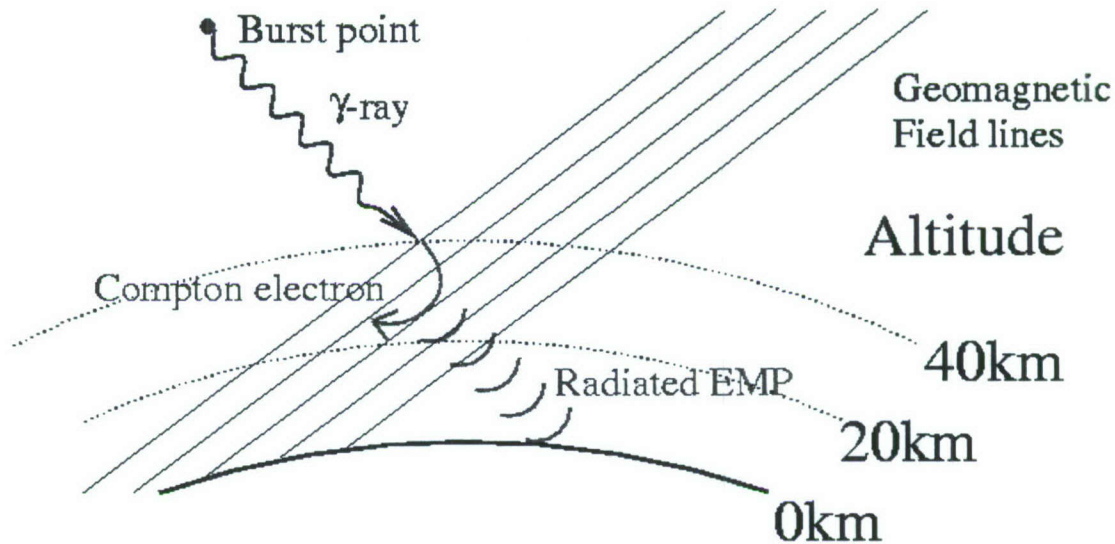
Figure 23. High altitude nuclear EMP [5].

The characteristics of this rapidly propagating energy pulse are:

- much of the energy is contained within a pulse (a short pulse-width);

- because of the short pulse-width, the pulse is likely to be thousands of volts/meter and hundreds of amps;

- most of the energy is probably contained in the fundamental resonant frequency of the explosion and for the first few harmonics of that frequency;

- a single pulse of high amplitude energy followed by a gradually diminishing pulse of energy that could last for minutes after the initial detonation.

From the energy-coupling models, the wavelength of the incident wave must be smaller than the length of the conductor or aperture that is carrying the damaging energy to the sensitive electronics. If the wavelength is not smaller than the conductor or aperture, then there will be little effective energy coupled to the electronics. The estimated frequency for HEMP is 1) up to 500 kHz for the initial pulse and 2) 500 kHz to 300 MHz for the long diminishing pulse. The wavelength corresponding to 500 kHz is 600 meters; the wavelength corresponding to 300 MHz (the trailing pulse) is 1 meter.

From this discussion, it is apparent that for HEMP, the damaging power could couple most effectively thorough long transmission lines. Electronics that are placed inside a metal enclosure and using a line filter would be relatively immune to the effects of HEMP.

High power microwave (HPEM) coupling characteristics

For narrowband high power microwaves (500 MHz to 5 GHz), the wavelength ranges from 0.6 meter to 0.06 meters. Choosing a representative frequency of 1 GHz, the wavelength would be 30 cm or approximately 1 foot. From coupling models, damaging energy could effectively couple to the electronics through an opening of six inches or less. Typical electronics enclosures have cabinet door openings and ventilation openings with openings much larger than six inches – for high power microwaves a metal cabinet would provide little protection to sensitive electronics. As will be demonstrated later, metal cabinets actually enhance the destructive effects of high power microwaves on electronics at resonant frequencies.

A recent study [6] has shown that *"although metal cabinets are often used to protect electronic equipment against electromagnetic interference ... the cabinet and printed circuit boards (PCB) inside form common mode (CM) circuits, which may influence the differential mode (DM) signal transmission on the boards and cause higher radiated emissions from the PCB"*.

The high power microwave energy can couple through small openings and apertures in the metal cabinet to the electronics that are placed inside. Additionally, the dimensions of the cabinet and the PCB's located inside can support a "standing wave" of high power microwave energy such that the electronics are illuminated with a new wave of damaging high power microwave energy during each successive microwave cycle. This characteristic of illuminating the electronics with a standing wave of high power microwave energy is known as 'pumping' energy into the enclosure. This characteristic is another argument in favor of a statistical electromagnetic description of the phenomenology.

High power microwave: local protective measures

A high power microwave device capable of generating energy damaging to the sensitive electronics in a building can be relatively small. New trends in pulsed power technology have led to compact devices. A device such as this can be placed in a shoulder carried bag or fitted into a suitcase. The capability of such a device is very high when placed in the proximity of the electronic devices, usually within tens of meters of the electronics. Larger high power microwave devices, mounted in a small moving van and fitted with an antenna, could also substantially damage electronics.

The choice of these high-risk targets involves interrupting or disabling the functionality of the target with little lethality to the occupants of the target. Since the target can be attacked from a location several kilometers from the target (for the highest power sources), the persons who are employing these devices are able to select targets that are more porous to the damaging high power microwave energy from the device. Unlike the employment of a high-altitude nuclear device by a military power, these high power microwave devices can be employed by anyone who has the financial or technological capability to construct or purchase such threats.

Likely targets for high power microwave threats

What would make the most likely target for high power microwave attack? In the recent past, terrorists over the world have targeted infrastructure. The train bombings in Spain, the subway bombings in England and in Japan, and the attacks on the World Trade Center all point to infrastructure targets.

These are some of the characteristics of these infrastructures that make them open to high power microwave attack:

- *"the high power microwave systems now under development occupy a frequency range between 500 MHz and 3 GHz, due primarily to the coupling effects and the generic electronic systems"*, so that the wavelengths of damaging energy range from 10 cm to 60 cm.

- microwave energy will pass through a frame-and-gypsum-board wall with little attenuation – however, a concrete or solid block wall about 8 inches thick will attenuate almost all microwave energy.

- window glass and other dielectric material have little effect on microwave energy. As will be shown later, special glass can be installed which will serve as shielding from microwave energy.

- large antenna structures, metal towers and masts, and metal decorative façade are often the structures that most readily support coupling of damaging energy into the building.

- exposed power or data lines routed into the building.

These are common characteristics of almost all the various types of commercial, residential, and industrial buildings in any particular area. In light of this fact, it is obvious that effective shielding methods must be implemented to reduce the effects of a possible high power microwave threat to critical infrastructure.

Whereas the terrorist attacks mentioned above had the intention of scaring the population at large and sought considerable publicity, their overall impact on the economy was small. A high power microwave attack, however, could be discrete, anonymous, and attract little publicity.

SECTION 3

DEGREE OF APPLICABILITY OF DIFFERENT MODELING APPROACHES

A variety of computational tools that could be used in an end-to-end modeling paradigm to study the effects of HPEM threats on critical infrastructure were investigated under this contract. The highlights are summarized here, in addition to results of the analysis supporting the Room 118 measurements using *Wireless Insite*.

The first computational tool that was evaluated and used as part of this study is JEM-RF [7]. JEM-RF estimates the 'hardness' of devices and systems to threats from narrowband RF threats. Inputs to the code are point sources and plane waves. The outputs are hardness (RF induced stress as a function of frequency); stress (defined as "damage" or "upset"); and strength (fields inside an enclosure, the voltage at a device pin, or the voltage on a wire connected to a port). The term "upset" covers interference, digital upsets, spoofing, or any other effect that does not involve direct RF damage. JEM-RF does not compute strength – it only computes stresses. The users provide strength data through a database or one can use some other model (such as microwave studio, FEKO, *etc.*).

The weak point of JEM-RF is that it models only narrowband signals. In addition, the strength levels of systems, devices, ports, *etc.* have to be known or calculated using another method. In terms of visualization, the code has limited capabilities (cannot see fields inside the device or a structure).

The next code that was evaluated was FEKO. This code is based on the Method of Moments (MoM). In FEKO the physical optics approach and the unified theory of diffraction are hybridized with the MoM for electrically large problems. The following excitations are possible in FEKO:

- Plane wave incidence
- Voltage source
- Pulses
- Electric and magnetic Hertzian Dipoles
- Aperture field as a source
- Point source
- Radiated power

The weak points of FEKO are in the scattering analysis. Whereas the accurate MoM can be used for the analysis of scattering from metallic or dielectric bodies up to several wavelenghts in size, electrically large problems, however, become impractical to solve with the MoM. In addition, the visualization capabilities are limited.

Wireless Insite models the effects of buildings and terrain on the propagation of electromagnetic waves. *Wireless Insite 2.0.5* is based on ray tracing and various

propagation models. In addition to JEM-RF, *Wireless Insite* was used most often in this study.

3.1 WIRELESS INSITE MODELING PERTAINING TO ROOM 118 EXPERIMENTS

Figure 24 presents a gain plot for a dipole antenna used as the transmitting antenna to replicate the Room 118 ECE Building experiments.
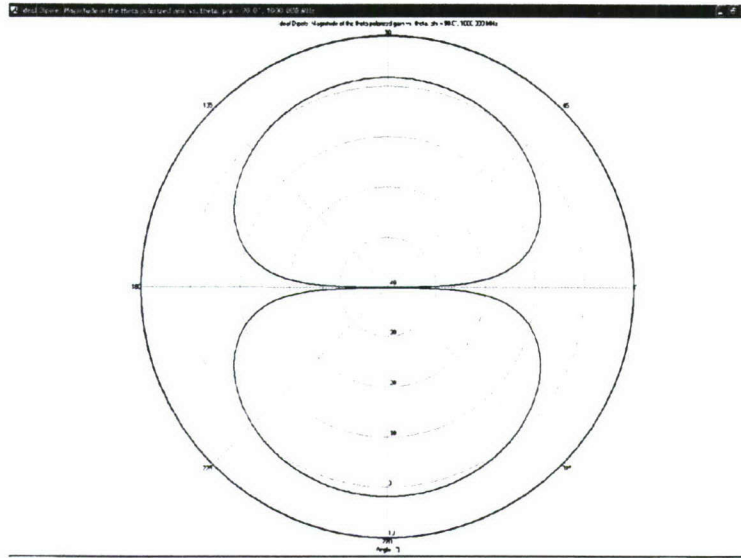
Figure 24. Gain plot for transmitting dipole antenna in Wireless Insite.

The mock-up for the Room 118 experiments is shown in Figure 25.
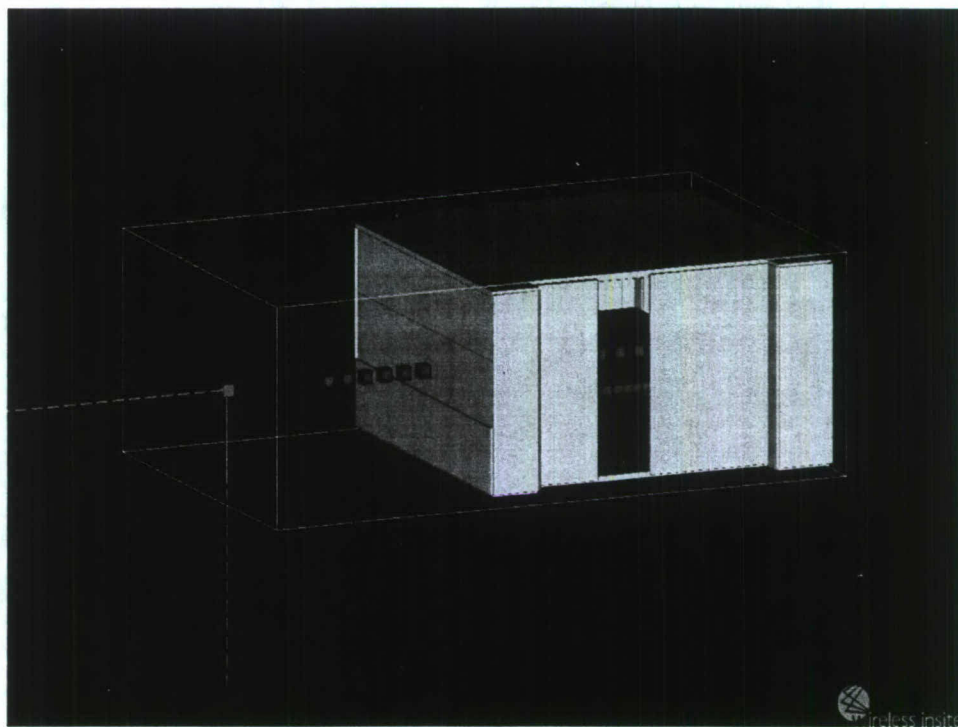
Figure 25. Mock-up of Room 118 experiments in Wireless Insite.

Figure 26 illustrates the location of loop receiver antennas used to receive the signal, and Figure 27 presents the received power distribution.
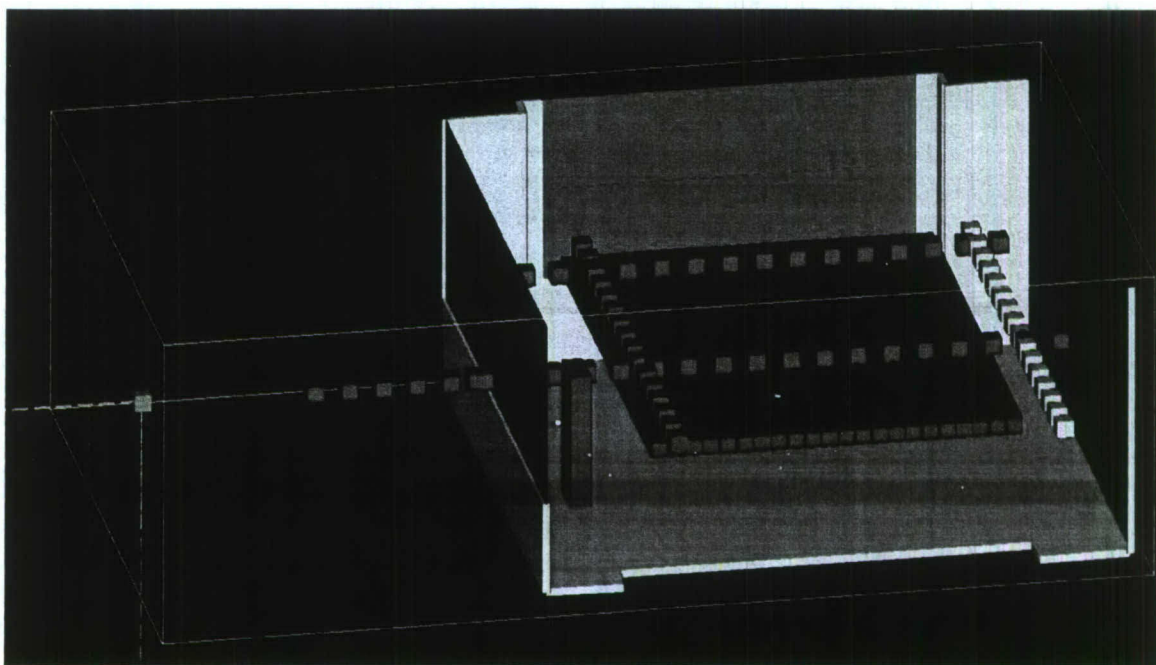
Figure 26. Location of loop receiving antennas distributed in the mock-up of Room 118 in Wireless Insite.
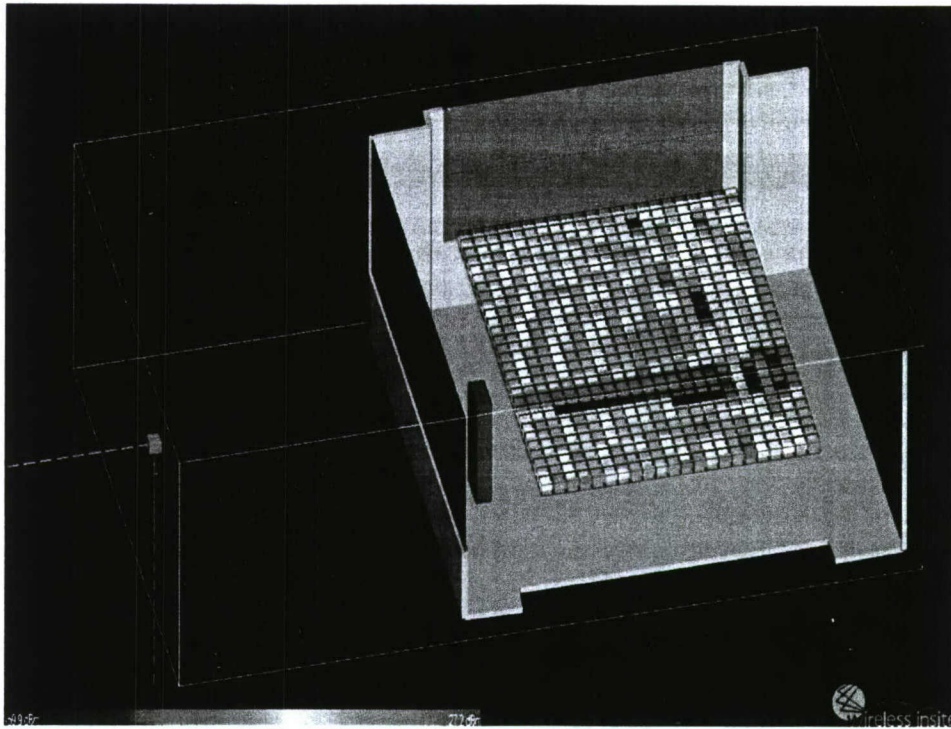
Figure 27. Received power in Room 118 mock-up calculated using Wireless Insite. (Red is the strongest and blue is the weakest.)

Figure 28 shows are vertical conducting bars are mocked-up in the simulation, and its effects on the received power are shown in Figure 29.
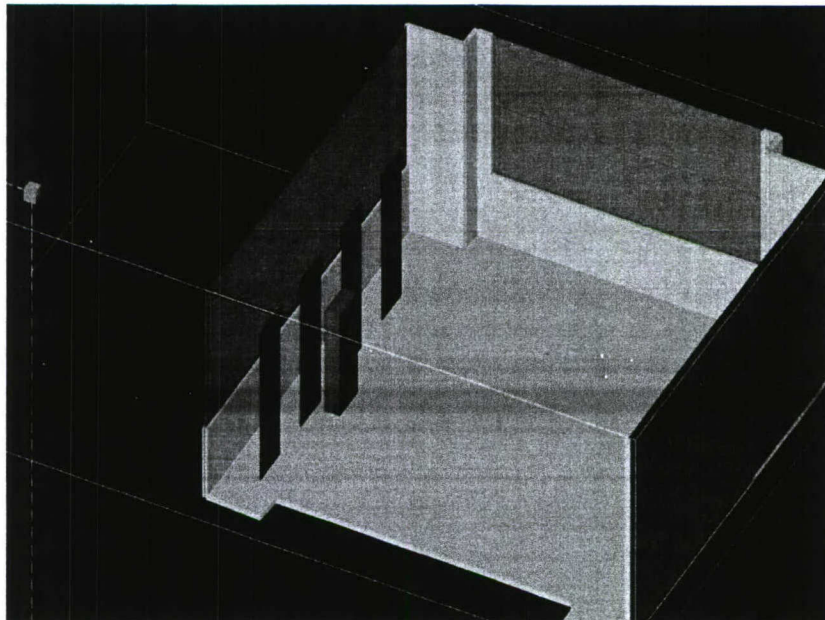
Figure 28. Vertical conductors are placed in the path of the incident radiation for the Room 118 simulations.
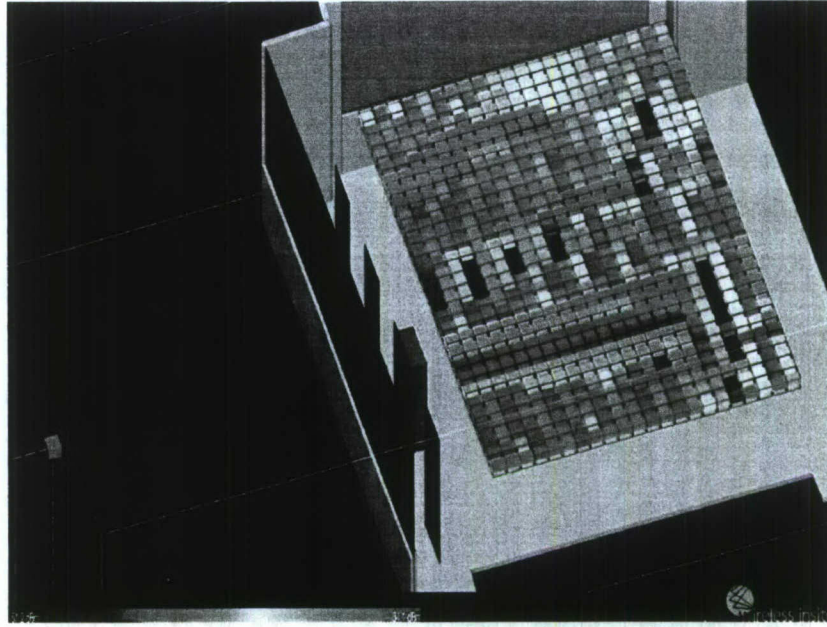
Figure 29. Received power in the presence of the vertical bars. This calculation can be compared with Figure 27.

Additional simulations will be continued to better understand the experimental measurements.[1]

---

[1] This ongoing work is being performed by C. Lambrinos as part of her M.S. thesis.

SECTION 4

NMSU RESEARCH ON MITIGATION PROTOCOLS

This research effort involved a collaboration with New Mexico State University (NMSU) on the study of the shielding effectiveness of various types of wall / window coverings.[2] The NMSU experimental set-up is shown in Figure 30. Wall coverings included wire mesh of various mesh sizes, paints that were advertised to offer effective shielding for microwaves, drywall, and aluminized-Mylar window tinting. An antenna was placed about 23 feet from a receiver that was housed in a shielded box. The box was fitted with a large opening over which was placed the various samples of the covering materials. Microwaves frequencies were generated and were swept from 400 MHz to 3 GHz; the received power was recorded in decibels, as shown in Figure 31, to give an indication of the level of the power received vs. the power transmitted.

Figure 30. Diagram of NMSU experimental set-up for characterizing shielding effectiveness of various materials against electromagnetic radiation in the frequency range of this study.

---

[2] A summary of NMSU data is presented in Appendix C.

Figure 31. Photograph of the NMSU test facility (left) and typical shielding effectiveness measurement data (right) for one particular material.

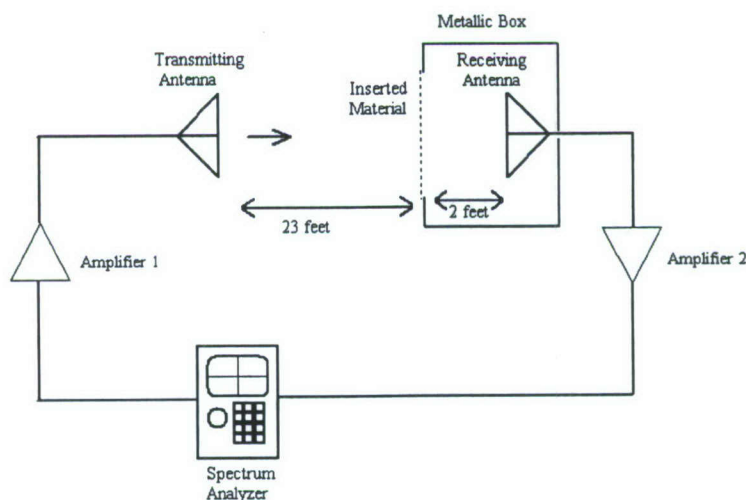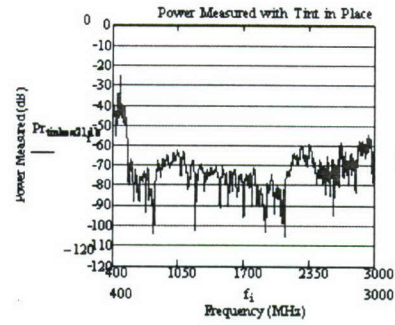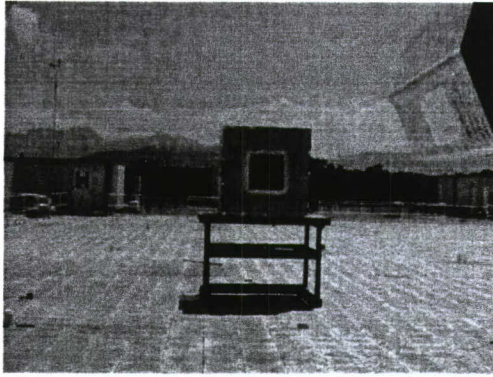## SECTION 5

COMPARISON OF UNM MEASUREMENTS AND MODELING RELEVANT TO UNM MEASUREMENTS

This Section presents a comparison of UNM modeling efforts, primarily using JEM-RF and Wireless Insite, with both UNM active measurments, and NMSU shielding effectiveness measurements.

5.1 JEM-RF OVERVIEW

JEM-RF [7] allows the user to enter a 'point source' or a 'plane wave' environment. In specifying a point source, propagation loss parameters such as line-of-sight distance, antenna gain, and some empirical models can be used in calculating the power incident at the electronic systems. For the research performed in this model, data from a test using a log-periodic antenna that broadcast a swept band of frequencies (200 MHz – 1 GHz) into room 118 at the ECE building at UNM was used (as shown earlier).

From the experimental data obtained in room 118, several resonance frequencies were chosen from the measured data. Applying the narrowband criteria (i.e., the bandwidth is < 1% of the center frequency), electromagnetic environment models were created in JEM-RF and applied to four models to determine frequency-dependencies in the models or data. Since the maximum power transfer occurs at the resonant frequencies, then the sensitive electronics would be at greatest risk at those frequencies.

5.2 RAY TRACING USING WIRELESS INSITE IN ROOM 118 MEASUREMENTS

Wireless Insite was used to demonstrate the effect of multipath propagation on the incident field strength of high power microwaves at various locations. Figures 32-34 demonstrate graphically the effect of multi-path propagation on the incident field strength of high power microwaves at the sensitive electronics. Figures 32 and 33 represent the propagation of electromagnetic radiation from the transmitting to the receiving antennas. Figure 34 is a measurement of the electric field at a position perturbed by the placement of a file cabinet (as was done during the measurements described earlier).
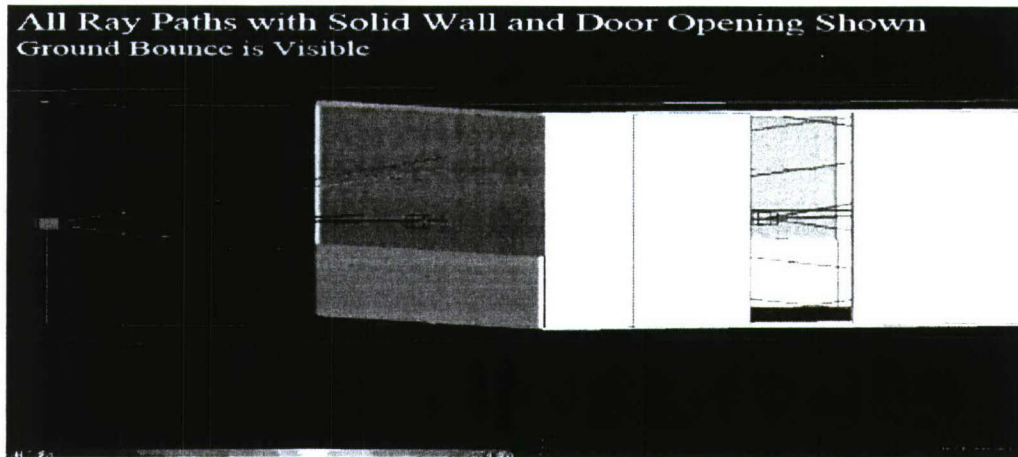
Figure 32. Wireless Insite calculation of the propagation of electromagnetic radiation through windows, doors, and walls.
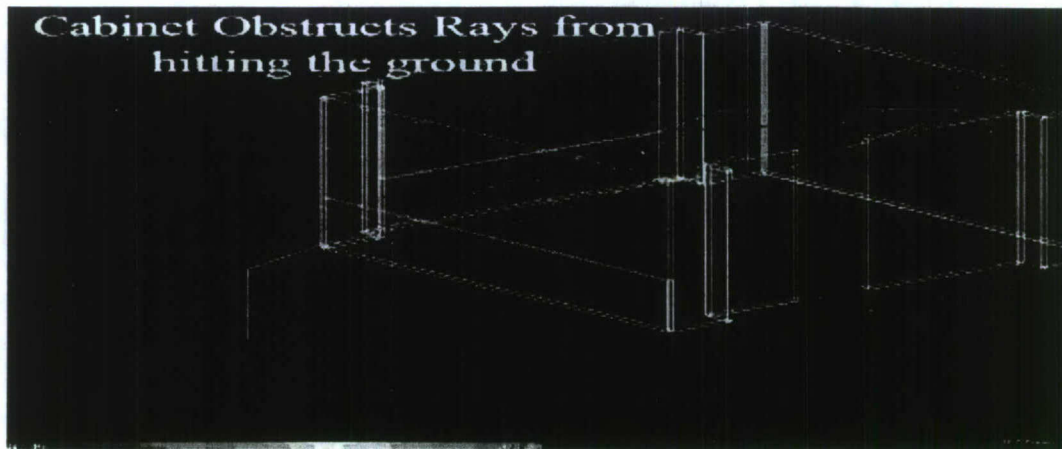
Figure 33. Wireless Insite calculation of the 10 'strongest' multi-path contributions to the energy in the mock-up of Room 118.
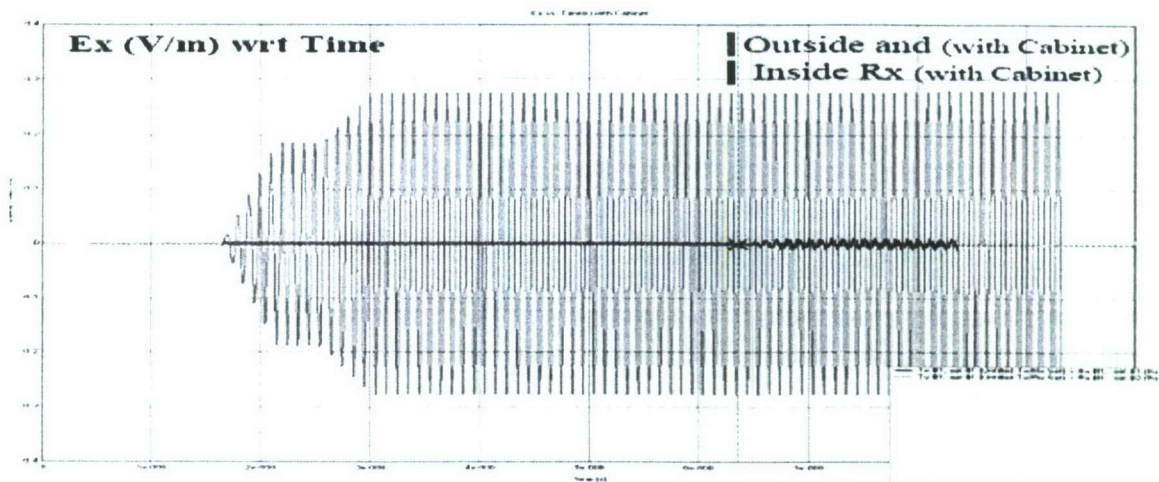
Figure 34. Wireless Insite calculation of the effect of a cabinet on the incident field strength in a mock-up of Room 118.

5.3 ENVIRONMENT SUMMARY GRAPHS IN JEM-RF

The ENVIRONMENT SUMMARY GRAPH tab shows three graphs, as shown in Figure 35. For this example, the environment in Enclosure1 is shown. For this model, Enclosure1 is the building in which the other enclosures and devices are placed. The building (Enclosure1) has no shielding and the other enclosures have varying levels of shielding. In this example *'CABINET w/Ferrite tile'*, with moderate shielding, is shown inside the building (Enclosure 1).[3]

---

[3] A comprehensive discussion of these can be found in P.Cravens, "Modeling and Mitigating High Power Microwave (HPM) Threats to Critical Infrastructure," M.S. Thesis, University of New Mexico, August 2006.

The electromagnetic environment inside the enclosure labeled *'ENV incident'* is shown in the first graph, the shielding effectiveness as a function of frequency of the enclosure labeled *'CABINET w/Ferrite tile'* is shown by the second graph, and the electromagnetic environment internal to *'CABINET w/Ferrite tile'* is shown in the third graph. Although the graph of the internal environment differs only slightly from the graph of the external environment, a close inspection will show that the amplitude of the internal environment is moderately less than that of the external environment.
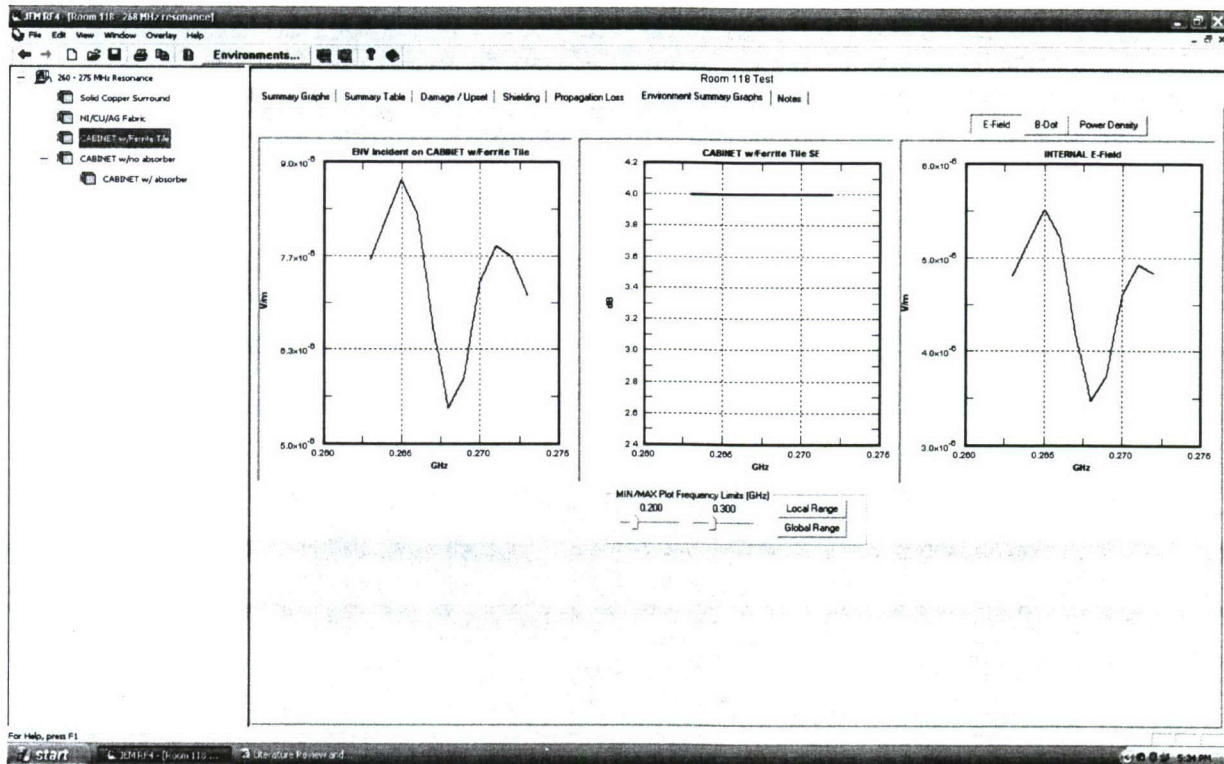
Figure 35. JEM-RF environment summary graphs.

The electromagnetic environments that were chosen were derived from the results of the testing previously mentioned. Each of the four subsequent electromagnetic environments was individually applied to the selected models and the corresponding Environment Summary Graphs were evaluated for frequency-dependence and attenuation of the incident wave amplitude. Three of the four models represent a steel electrical cabinet measuring 24 X 36 X 36 inches which has modeled spacings around the door and two (1/4") circular openings for data and power lines. These three modeled steel cabinets were assigned an appropriate conductivity and were lined with different types of liners: 1) 6" ferrite tile, 2) no absorber material, and 3) 12" absorbing cones. Additionally, the cabinets were modeled with (4) 6 X 9 inch circuit card assemblies for device rectification of the incident wave. The remaining enclosure was modeled as (4) 10 ft X 10 ft fabric panels using a commercial EMC reduction fabric (nickel – copper - gold), which advertises 80 dB attenuation.

The Environment Summary Graphs in Figure 36 do not show any significant frequency-dependence for the selected frequency bands, but all graphs do show a significant reduction in amplitude, especially with the NMSU testing data.
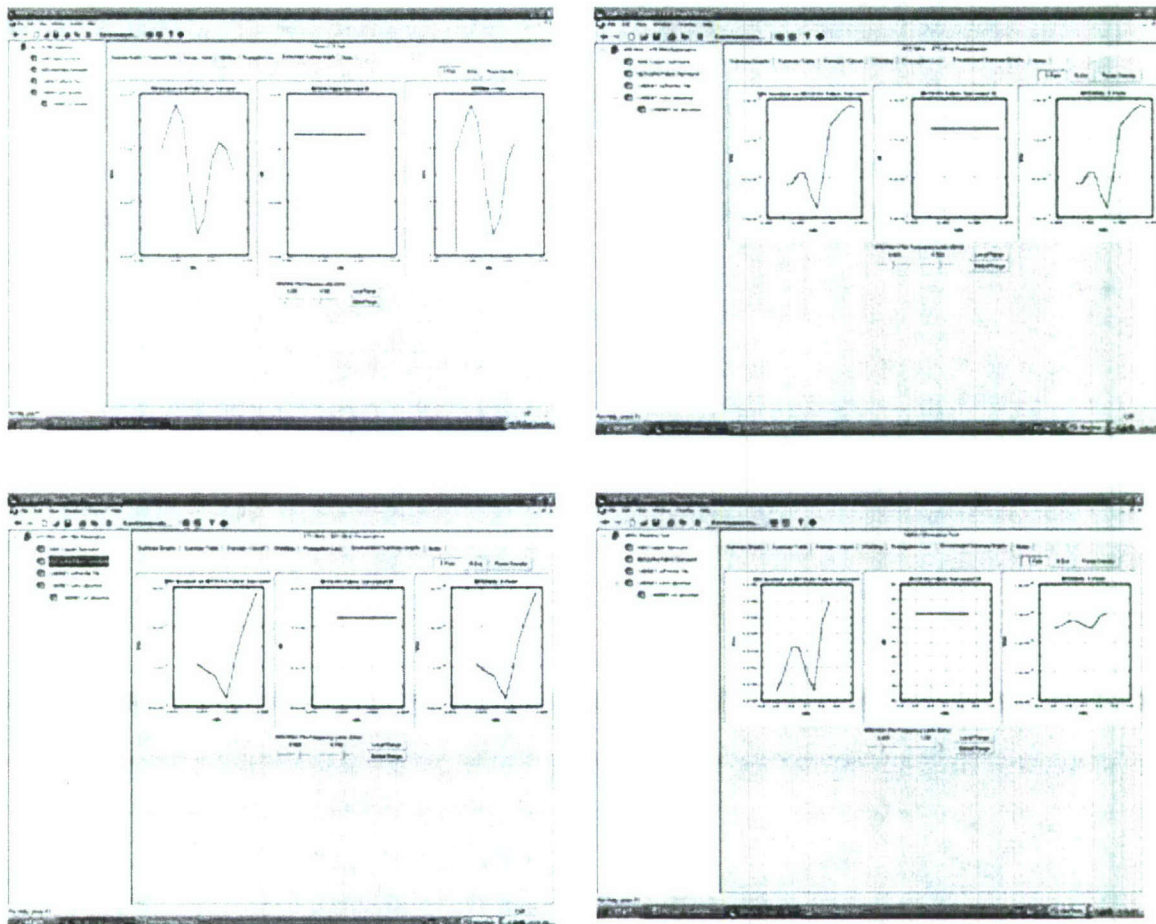
Figure 36. Nickel-copper-gold fabric surrounding. (Top left is 260 MHz-275 MHz resonance; top right is 455-475 MHz resonance; bottom left is 674 MHz-684 MHz resonance; bottom right is NMSU test data.)

For the electromagnetic environments applied to the steel cabinet lined with 6" ferrite tile, shown in Figure 37, none of the internal environments showed any frequency-dependent response to the incident wave. The ferrite tile was rated at 4 dB attenuation; however, the reduction in the various internal environments only showed about a 30% reduction in the amplitude.

Figure 37. Steel cabinet w/ 6" ferrite tile. (Top left is 260 MHz-275 MHz resonance; top right is 455-475 MHz resonance; bottom left is 674 MHz-684 MHz resonance; bottom right is NMSU test data.)

For Figure 38, three of the internal Environment Summary Graphs showed no significant attenuation of the incident wave energy. For the internal environment depicted by the 455 MHz – 475 MHz resonance, the attenuation decreased from 4.2 dB to 3.2 dB and the corresponding internal environment showed about a 30% reduction in amplitude from the external environment. The attenuation for the three other frequency bands averaged much less than unity.

Figure 38. Steel cabinet w/no absorbing material. (Top left is 260 MHz-275 MHz resonance; top right is 455-475 MHz resonance; bottom left is 674 MHz-684 MHz resonance; bottom right is NMSU test data.)
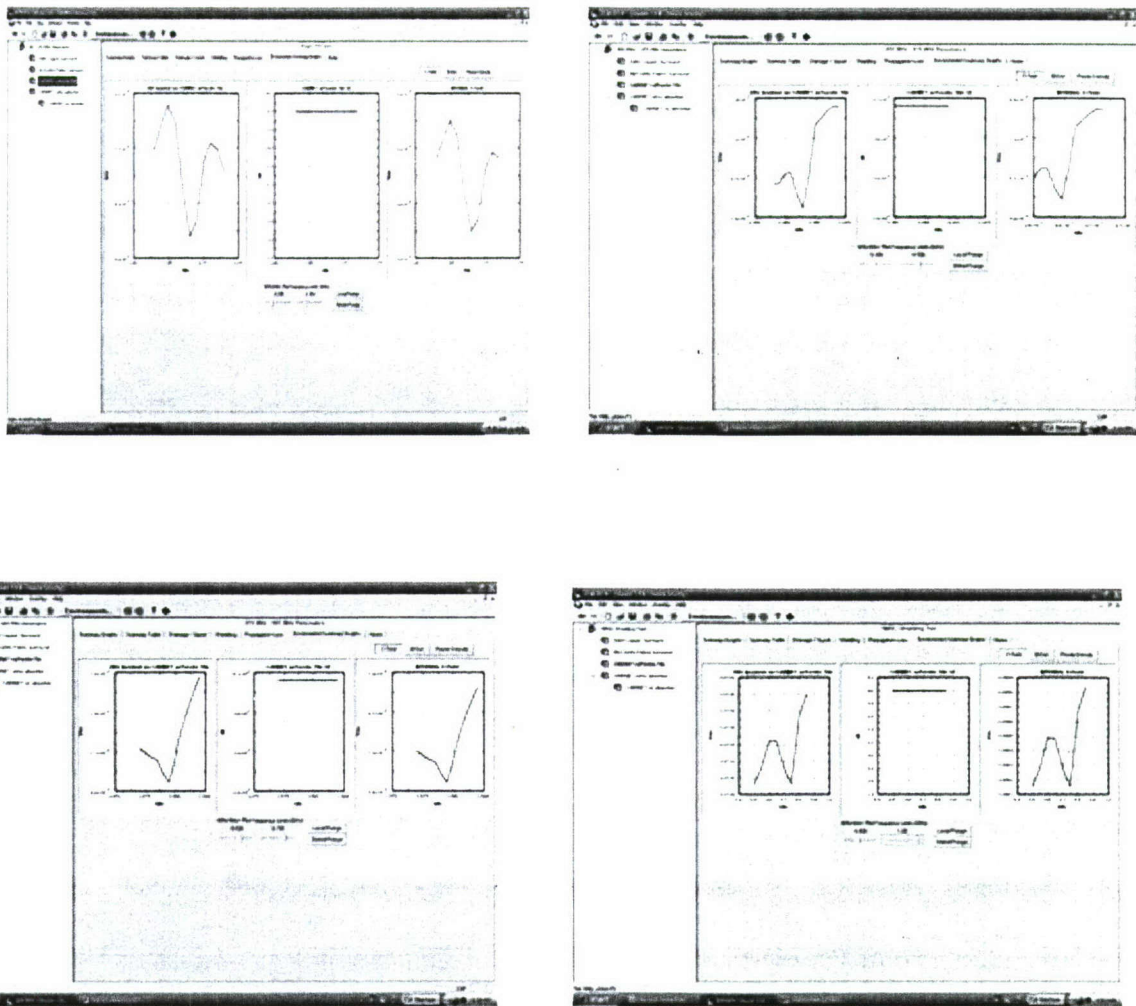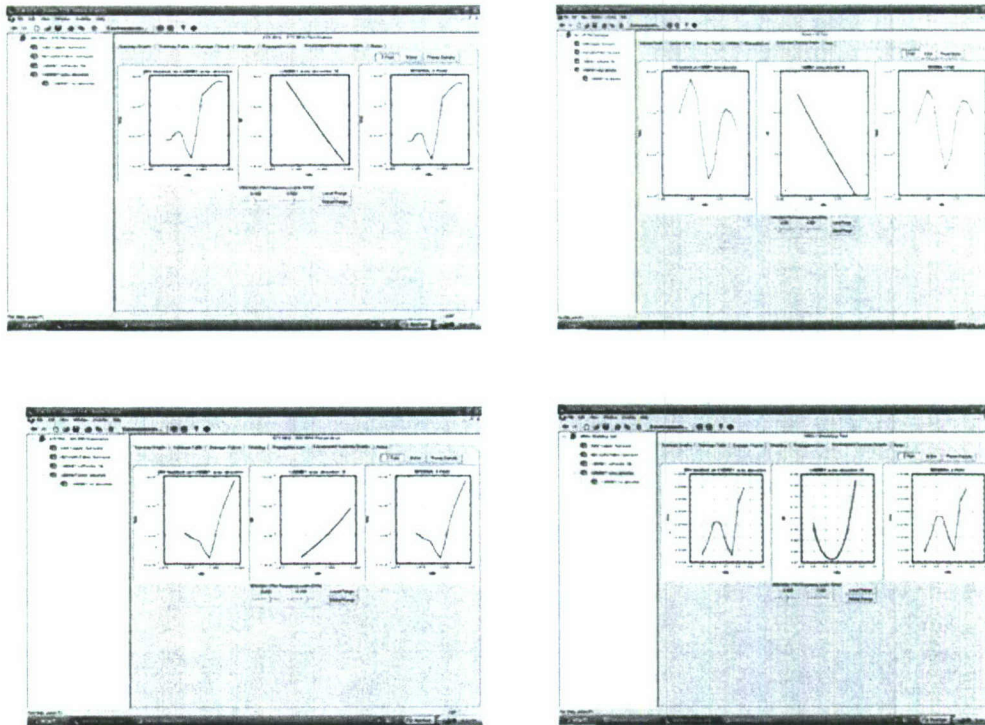
Figure 39. Steel cabinet w/ 12" absorbing cones. (Top left is 260 MHz-275 MHz resonance; top right is 455-475 MHz resonance; bottom left is 674 MHz-684 MHz resonance; bottom right is NMSU test data.)
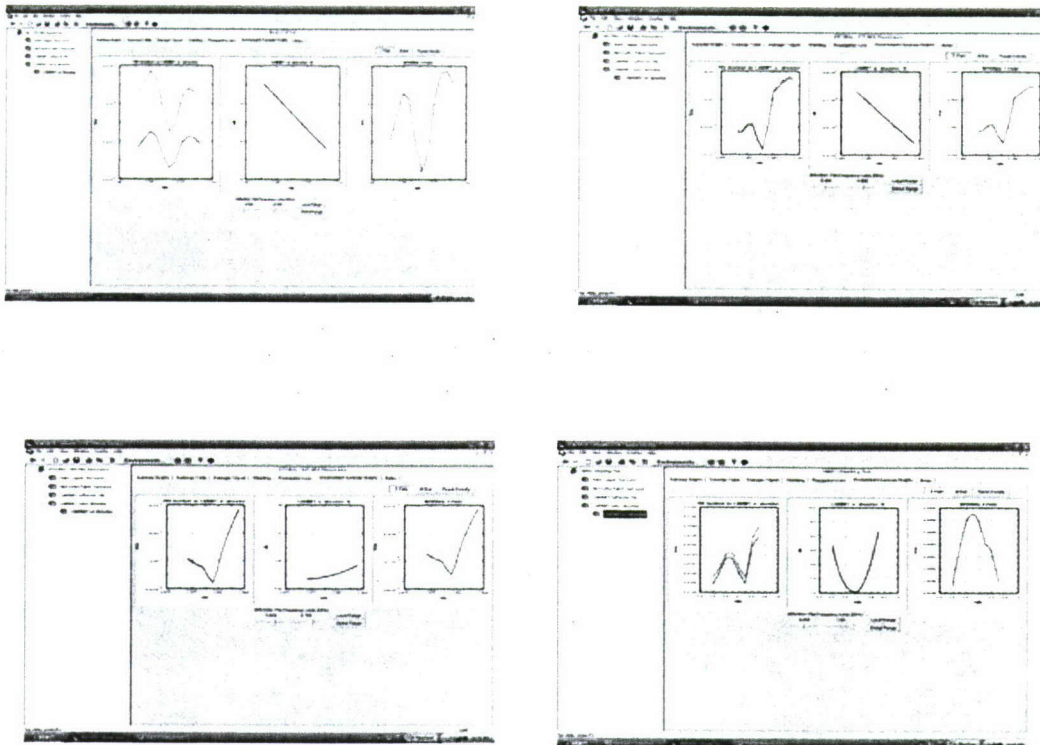
For the steel cabinet lined with absorbing cones, the attenuation was twice that for the steel cabinet without absorbing material. For the lower range of frequencies, there was 26 dB attenuation. For the middle range of frequencies, the attenuation was constant at 7 dB, for the higher range of frequencies the attenuation was about 9 dB. The reduction averaged about 60% for all the environments except the low frequencies, which diminished significantly.

5.4 INCREASING SHIELDING EFFECTIVENESS USING NESTED ENCLOSURES

JEM-RF has good modeling capability by the use of 'nested enclosures' to determine an appropriate and cost-effective method to safeguard the sensitive electronics against the threat of high power microwaves. To develop an effective model, the user models a number of enclosures representing various interior rooms and possible shielding configurations for each of those rooms. Each enclosure is 'transparent' to the electromagnetic environment until shielding configurations are specified for the enclosure. After the user has determined the number of interior rooms, and the corresponding number of enclosures to model using JEM-RF, the user determines the acceptable field strength for the sensitive electronics that are being shielded.

A simple model of a "financial center" having various interior rooms was developed, and the sensitive electronics are enclosed in a standard steel cabinet. The Environment Summary Graphs in Figures 40, 41, and 42 represent the incident hypothetical high power microwave field strength, the shielding effectiveness of the cabinet, and the resulting internal electromagnetic environment.

Figure 40 represents a high power incident wave upon a modeled steel cabinet. The second graph shows a definite frequency dependence of the steel cabinet and the enclosed circuit card assemblies and the third graph shows the modeled internal environment. The effect of frequency dependence of the enclosure on the incident waveform is clearly depicted in this third figure, as is the attenuation of the amplitude of the incident wave by the enclosure.
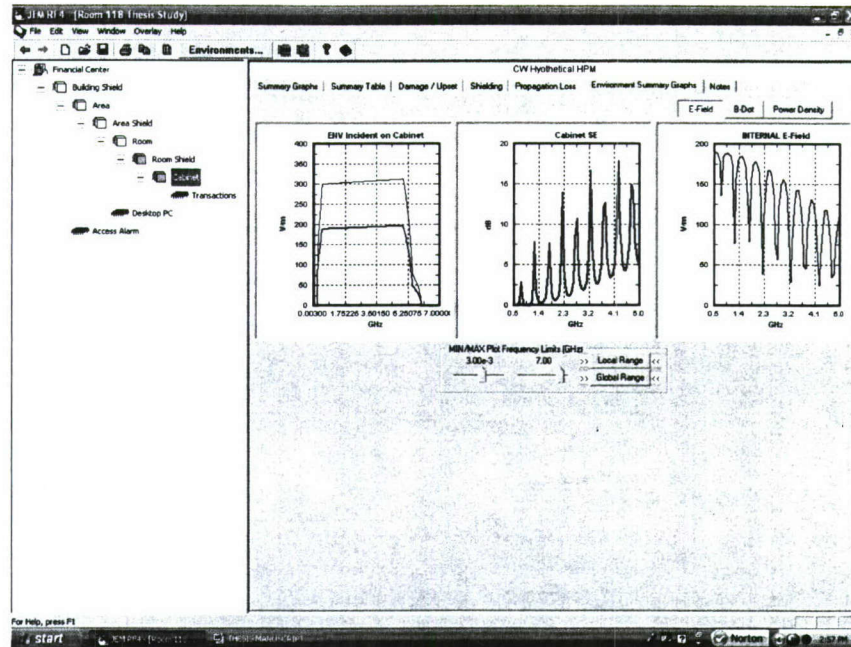
Figure 40. Environment Summary Graphs for steel cabinet.

Figure 41 represents the addition of a modeled enclosure surrounding the initial enclosure. This second enclosure has a specified attenuation of 4 dB and the result of that attenuation is depicted in the respective graphs. It is clear that the frequency dependence of the enclosure has not changed.
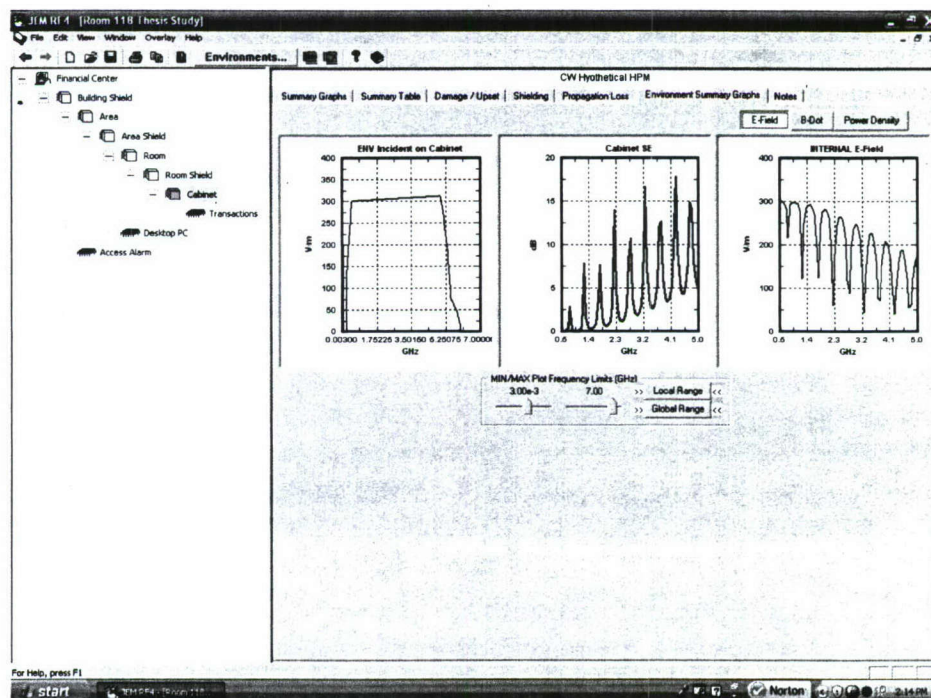

Figure 41. Environment Summary Graphs for steel cabinet after additional 4 dB room shield.

Following the progression of modeling additional enclosures representing additional shielding configurations, the effect of adding these additional shielding configurations can be determined. This model can be used to identify locations and materials that would be necessary to affect a shielding configuration for the entire building, and provide protection for all sensitive electronics at the appropriate shielding effectiveness for each location. From the Environment Summary Graph in Figure 42, it is plainly seen that additional levels of protection can be effectively modeled with each new shielding configuration until the acceptable incident field strength is reached at the sensitive electronics.
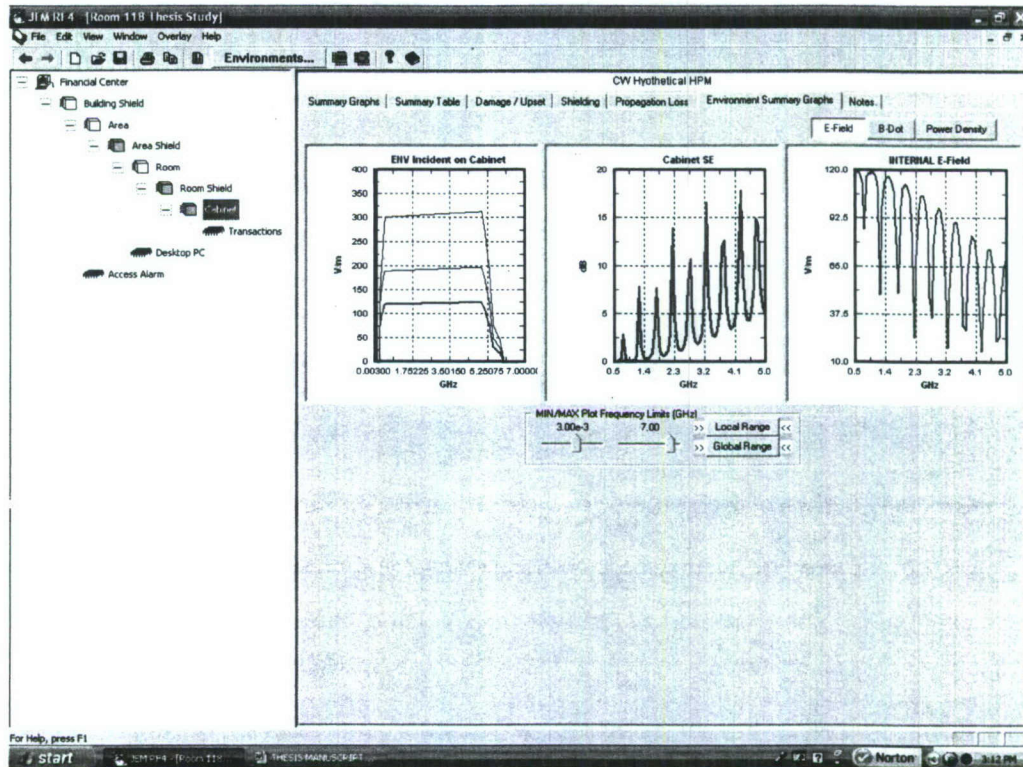

Figure 42. Environment Summary Graphs for steel cabinet after 2nd addition of 4 dB room shield.

Figure 43 below shows the "peak O. C. voltage" and the frequency at which it is effectively coupled to the conductors on the PCB's. This graph shows the modeled voltage that is coupled to the conductor at the device that is specified by the user. For this example, the user finds that 1.77 V is coupled to the conductor at a frequency of 1.9 GHz. The user can determine whether this modeled voltage is acceptable or whether additional shielding needs to be configured for these electronics.
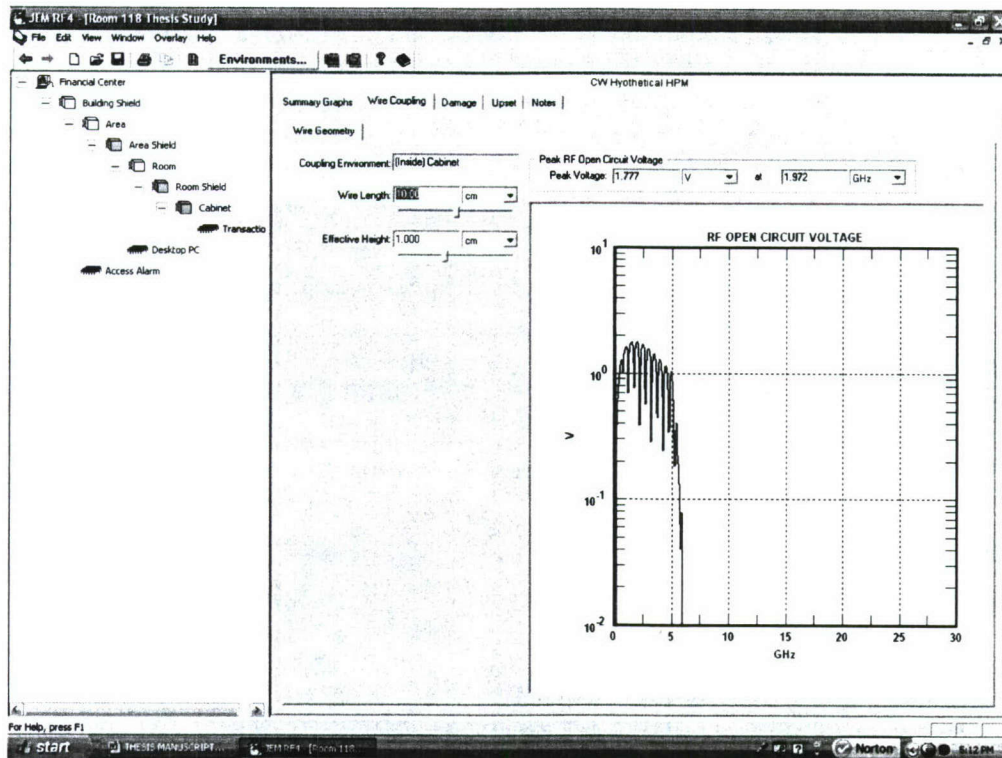
Figure 43. Wire coupling graph showing peak O.C. voltage.

SECTION 6

INTEGRATION OF STATISTICAL ELECTROMAGNETICS WITH DETERMINISTIC MODELING

The results of both experimental testing (particularly the active measurements in ECE 118) and computational modeling (particularly using the ray-tracing code Wireless Insite and the JEM RF stress-strain code) suggest that it will never be possible to completely understand the electromagnetic environment that is under threat. With the assumption that the cavity is "chaotic," however, one can use the recently developed theory of wave chaos to characterize how electromagnetic radiation is distributed in an enclosure.

6.1 OVERVIEW OF STATISTICAL ELECTROMAGNETICS

The problem of the coupling of electromagnetic radiation in and out of structures is a general one which finds applications in a variety of scientific and engineering contexts. Examples include the susceptibility of circuits to electromagnetic interference, the confinement of radiation to enclosures, as well as the coupling of radiation to accelerating structures [8–11]. Because of the wave nature of radiation, the coupling properties of a structure depend in detail on the size and shape of the structure, as well as the frequency of the radiation. In considerations of irregularly shaped electromagnetic enclosures for which the wavelength is fairly small compared with the size of the enclosure, the electromagnetic field pattern within the enclosure, as well as the response to external inputs, is very sensitive to small changes in frequency and to small changes in the configuration. Thus, knowledge of the response of one enclosure configuration may not be useful in predicting that of a second nearly identical enclosure. This motivates a statistical approach to solving this electromagnetic problem.

A brief overview is presented as follows. The purpose of this approach is to develop a statistical model for predicting the impedance characteristics of a chaotic cavity. The cavity is called "chaotic" because its geometry causes input electromagnetic waves to behave in a random fashion, thus creating randomized input impedance characteristics for the cavity. An illustration of a chaotic cavity is given as Figure 44.
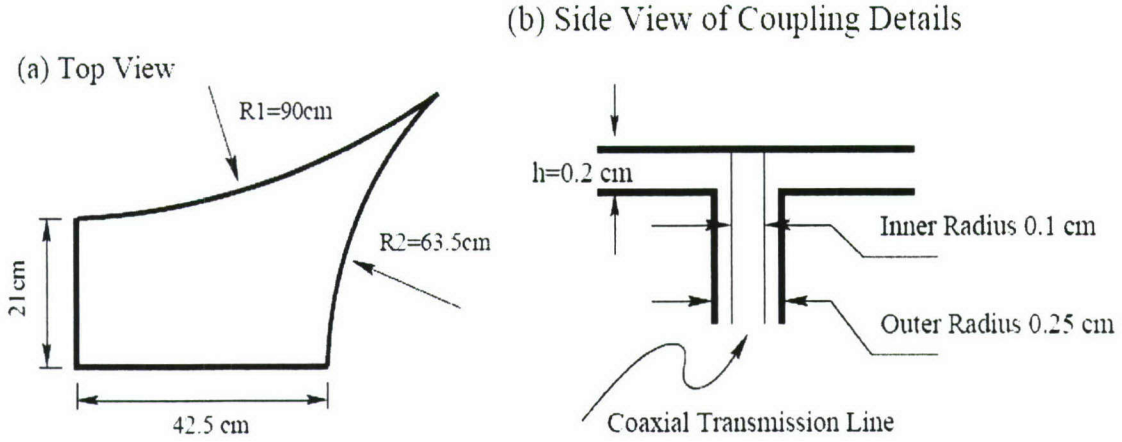
(a) Top View
(b) Side View of Coupling Details

R1=90cm

R2=63.5cm

21 cm

42.5 cm

h=0.2 cm

Inner Radius 0.1 cm

Outer Radius 0.25 cm

Coaxial Transmission Line

Figure 44. Top and side views of a chaotic cavity.

The impedance characteristics of a chaotic cavity can be described with chaotic eigenfunctions in the system's input impedance matrix. Analysis has shown that these matrices of chaotic eigenfunctions exhibit behavior described by what is called Random Matrix Theory. This theory applies to generalized, or "universal", systems. A universal system is one that does not incorporate any specific properties, such as the configuration of the port connecting the cavity to the transmission line and the type of transmission line used. These system specific properties of the cavity are added to the system mathematically with the use of the Poisson Kernel. Within the cavity, the ray trajectories of the electromagnetic waves are chaotic, and the distribution is modeled by a superposition of isotropically propagating plane waves. This model is called the Random Plane Wave Hypothesis.

The cavity can be described by:

$$\hat{V} = Z\hat{I}$$

$$\hat{V} = -j\sum_n \frac{kh\eta_0 \langle u\phi_n \rangle^2}{k^2 - k_n^2}\hat{I} = Z\hat{I}.$$

$$\phi_n = \lim_{N \to \infty} \sqrt{\frac{2}{AN}} Re\{\sum_{j=1}^{N} \alpha_j \exp(ik_n \vec{e}_j \cdot \vec{x} + i\theta_j)\}$$

where k and k_n are wave numbers, h is a property of the cavity shown in Figure 44, η_0 is the characteristic impedance of free space, u is a quantity describing the vertical current distribution at the input port, and ϕ_n are the chaotic eigenfunctions. The impedance and scattering matrices can then be related by

$$S = Z_0^{1/2}(Z + Z_0)^{-1}(Z - Z_0)Z_0^{-1/2}$$

The statistical properties of a cavity are derived from its radiation impedance, which is a measured quantity. The coupling of energy into the port depends on both the geometry of the port and the geometry of the cavity. These effects can be separated to obtain universal properties for the system. To get this universal quantity (ξ), the measured radiation impedance must be used. This radiation impedance is normalized by subtracting the radiation reactance, and normalizing to the radiation resistance. This is given by

$$\xi = \{\mathrm{Im}[Z(k)] - X_R(k)]\}/R_R(k)$$

For this system given in Figure 44, this process was completed by measuring the cavity's radiation impedance and obtaining ξ. These values were then compared to Monte Carlo prediction and simulation using HFSS. The results are shown below in Figure 45 for different frequency ranges, and good agreement is seen for all frequency ranges.
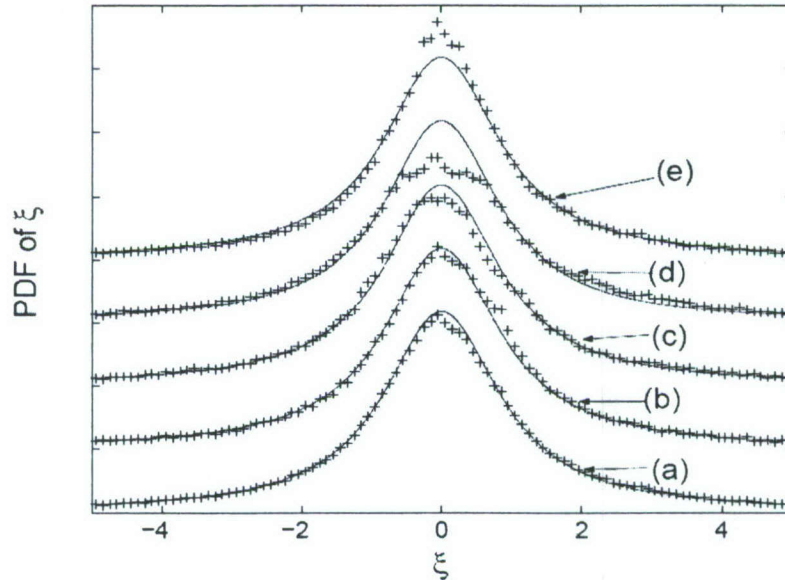

Figure 45: Histogram approximation to $P_\xi(\xi)$ calculated using HFSS in different frequency ranges: (a) 6.75-8.75 GHz, (b) 6.75-7.25 GHz, (c) 7.25-7.75 GHz, (d) 7.75-8.25 GHz, (e) 8.25-8.75 GHz.

Some important findings of this wave chaos approach include that the impedance characteristics of the system can be separated into effects relating to the geometry of the port, and those related to the geometry of the cavity. The impedance characteristics of the cavity can be treated in a statistical way using random matrix theory. These universal aspects of the system can be obtained by measuring the cavity's radiation impedance, while system-specific properties are added through the use of the Poisson Kernel. In simulation, the impedance is Lorentzian distributed with a mean equal to the radiation reactance, and a width equal to the radiation resistance, and simulated results using the statistical model agree with measured quantities.

In summary, it is anticipated that an end-to-end modeling paradigm would comprise the following aspects:

i)   use of codes such as Heimdall to predict the output of an HPEM threat;

ii)   use of a propagation code, such as *Wireless Insite* to calculate the propagation of the EM energy, and its coupling to a facility (a chaotic cavity);

iii)   use a statistical EM approach, as illustrated in Figure 46, to assess the distribution of EM energy in a chaotic cavity.

iv)   statistical EM could be used to further consider a sub-cavity (such as a computer, network, or enclosure) within the facility, and JEM-RF could be used to complement the analysis.
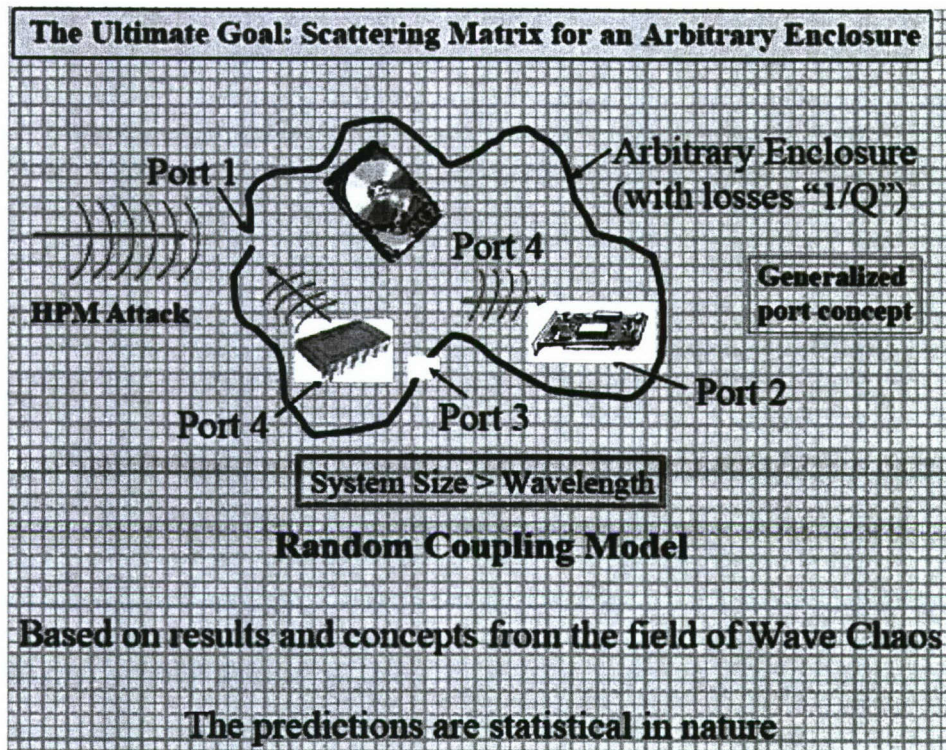
Figure 46. A modeling paradigm summarizing the use of the Random Coupling Model and Scattering Matrix to assess the distribution of EM fields in a chaotic cavity.

SECTION 7

CONCLUSIONS

With the entrance of sophisticated electromagnetic threats, there also comes a responsibility to reconsider the manner in which these new threats are investigated and mitigated. Most of the software and hardware solutions that have been developed are deterministic in nature and may not be adequate to accurately assess the nature of the threats.

There is a growing realization that attacks and warfare may be localized urban warfare rather than the traditional battle scenarios that involve large theaters of operations. Because there have been new non-lethal weapons introduced into our society and because our research indicates that we are unprepared for these types of attacks and unprotected against these new weapons, resources that can accurately consider the problem need to be developed.

There were several lessons learned in studying this problem. There is a need to model the electromagnetic environments from a statistical perspective so that more general solutions may be developed and applied to various scenarios. Most of the modeling relies too heavily on fixed placement of interior structures such as cabinets, walls, and infrastructure. Researchers, such as the ones at the University of Maryland, are using 'wave chaos' to effectively derive models for interior rooms, regardless of the spatial orientation of the contents of the room [2].

Regardless of the method by which the field strength is determined for a critical infrastructure, the acceptable field strength must always be determined to adequately protect sensitive electronics. Because of this fact, there will always be a need for a program such as JEM-RF to determine the amount of damaging energy that may be coupled to the sensitive electronics and there will be a need for a program to determine an acceptable shielding solution for sensitive electronics. JEM-RF has tremendous capabilities for modeling the acceptable energy, for modeling acceptable shielding solutions, and for modeling propagation losses based on widely-accepted empirical models of propagation.

As was mentioned previously, JEM-RF will need high-level processors and large amounts of workspace memory to accurately model these parameters in a timely manner. As the costs of computers and memory are continuing to decrease, that constraint of JEM-RF becomes less substantial. The program takes an investment of time to properly learn to use, but the development of accurate numerical models to compute the field strengths and electrical pin stresses would be an overwhelming task.

An end-to-end modeling paradigm, beginning with the launch of electromagnetic radiation and determining its consequences, and incorporating statistical electromagnetics, will be important for the protection of our critical infrastructure.

SECTION 8

REFERENCES

1. A.E. Motter and Y.-C. Lai, "Cascade-Based Attacks on Complex Networks," Phys. Rev. E., vol. 66, 065102 (2002). (UNCLASSIFIED)

2. See, for example, C.D. Taylor and D.V. Giri, *High-Power Microwave Systems and Effects* (Taylor & Francis, Washington, DC, 1994). (UNCLASSIFIED)

3. See, for example, X. Zheng, T.M. Antonsen, Jr., and E. Ott, "Statistics of Impedance and Scattering Matrices in Chaotic Microwave Cavities: Single Channel Case," Electromagnetics, vol. 26, 3 (2006); X. Zheng, T.M. Antonsen, Jr., and E. Ott, "Statistics of Impedance and Scattering Matrices of Chaotic Microwave Cavities with Multiple Ports," Electromagnetics, vol. 26, 37 (2006), and references therein. (UNCLASSIFIED)

4. R.A.Roussel-Dupre', "Prompt HEMP and Synchrotron Radiation: A Resolution of Two Approaches," IEEE Trans. Electromagnetic Comp., vol. 47, No. 3 (2005). (UNCLASSIFIED)

5. http://www.awe.co.uk/Images/emp(transparent)_tcm6-1599.gif (UNCLASSIFIED)

6. A.P.J von Deursen and S. Kapora, "Coupling Effects and Radiation of a 3-layer PCB on top of a metal cabinet," IEEE Trans. Electromagnetic Comp. Vol. 47, No. 3 (2005). (UNCLASSIFIED)

7. Titan Advanced Technology Group – Radio Frequency Protection Techniques Division, JEM RF USER'S GUIDE version 4; Jaycor SB04 (2004). (UNCLASSIFIED)

8. X. Zheng, *Statistics of Impedance and ScatteringMatrices in Chaotic Microwave Cavities: The Random Coupling Model*, Ph.D. Dissertation, University of Maryland (2005). (UNCLASSIFIED)

9. T.H. Lehman and E.K. Miller, Conference Proceedings: Progress in Electromagnetics Research Symposium, Cambridge, MA, July 1–5, 1991, p. 428. (UNCLASSIFIED)

10. J.G. Kostas and B. Boverie, IEEE Trans. EMC 33, 366(1991). (UNCLASSIFIED)

11. R. Holland and R.St. John, Conference Proceedings: 10th Annual Review of Progress in Applied Computational Electromagnetics, Monterey, CA, March, 1994, vol. 2, p. 554–568. (UNCLASSIFIED)

Appendix A

Sample Measurements for HPEM Assessments of Buildings

By

Dr. F. M. Tesche, EMConsultant
Dr. D. V. Giri, Pro-Tech

March 5, 2005

Summary

This memo describes a continuous wave (CW) test method for obtaining transfer functions between an antenna illuminating a building or other facility and the internal magnetic fields, which are induced by the antenna. Typical CW transfer functions measured in an actual facility are illustrated, and the various uses of these transfer functions are mentioned. Finally, at the end of this memo there are several calculations suggested that may be beneficial to the students who will be working on the measurements for this Defense Threat Reduction Agency (DTRA) program. The measured transfer functions used in this memo have been provided digitally.

Contents

Figures

Sample Measurements for HPEM Assessments of Buildings

1. Introduction

For assessing the effects of high power electromagnetic (HPEM) effects on buildings and facilities of interest to the Defense Threat Reduction Agency (DTRA), it is necessary to characterize the internal electromagnetic (EM) field distribution within the facility enclosure where sensitive equipment might be located. While there are a number of commercially available EM analysis codes that can be used to predict the penetration of external EM fields into a facility, it is generally recognized that measurements performed on such a facility provide a more accurate knowledge of the fields. Accordingly, in the current project being conducted by UNM for DTRA, internal field measurements are suggested to gather the needed data for use in the assessment of internal equipment.

Because the exact facility for this assessment has not yet been approved by DTRA, and because such field measurements are well in the future, it is desirable to obtain some "sample" data that is similar to what would be obtained in the actual measurement program. This will illustrate the type of data, how it is obtained with the measurement equipment, and provides an opportunity to develop analysis procedures for reducing and displaying the measured data.

In performing EM measurements on a facility, there are two basic approaches that can be envisioned. Both of these test methods are described in an IEC Standard [1]. The first method is to use a transient field measurement, where the facility is illuminated by a wide-band pulsed signal and the resulting internal transient fields are measured. Technology for performing these measurements has been developed over the last 40 years in the area of nuclear electromagnetic pulse (NEMP) assessment.

Alternatively, measurements can be conducted in the frequency domain, where a time-harmonic or continuous wave (CW) signal is used to illuminate the facility and the internal fields are measured. The test frequency is swept from a low frequency to a suitably chosen high frequency, and the internal fields are then characterized within this band of frequencies. In this CW measurement approach, both magnitude and phase of the internal fields are required (as opposed to magnitude-only measurements that are common in electromagnetic compatibility (EMC) testing.)

For this latter measurement approach, it is common to represent the facility behavior as a complex-valued, frequency dependent transfer function, which relates the internal E or H field to a measured external reference quantity, such as an incident E-field or the excitation voltage on an illuminating antenna. More will be said about this later.

Transient measurements and CW measurements on a facility are related through the Fourier transform. Thus, in principle it is necessary to perform only one type of test to characterize the facility. Each test has its own set of benefits and difficulties, including ease in

measurement, noise characteristics, portability of equipment, etc. The main benefit of the transient measurements lies in the fact that the entire transfer function as a function of frequency is obtained by a single shot pulse measurement, followed by a numerical Fourier transform. However, in the proposed DTRA testing, the CW test approach is envisioned. This is due to the fact that this type of testing can be performed at relatively low power levels (to minimize the possible interference effects on nearby equipment), yet while still providing adequate measurements in reasonably well-shielded facilities.

In this memo, sample CW transfer function measurements that were taken on a rebar-reinforced concrete building are described and data processing requirements are outlined.

2. Test Description

As outlined in Section 1, the CW measurements involve illuminating the building by an external EM source (antenna) and then measuring the internal EM field. Figure 1 shows the facility used in this test, along with the external antenna – the so-called "impulse-radiating antenna" (IRA). This antenna was initially designed for radiating a clean impulse-like transient EM field, but it also functions as a CW radiator with a very large operating range of frequencies. It offers superior performance over the standard EMC antennas.
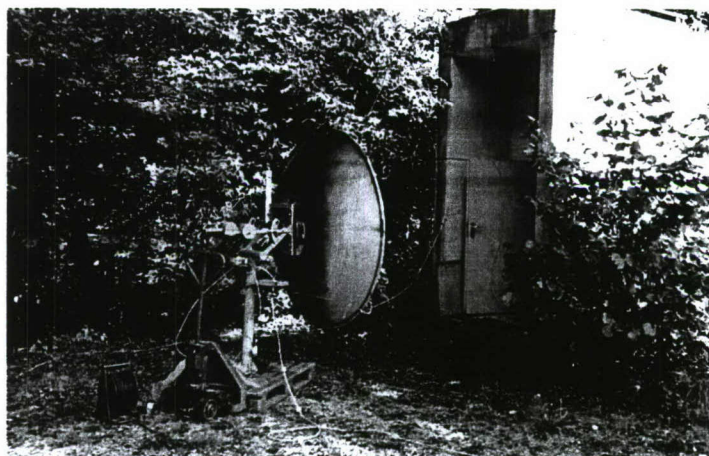
Figure 1. Illustration of the IRA located at the facility entrance.

This IRA radiator uses the standard parabolic design, which is shown in Figure 2. The antenna dimensions are as follows:

- D = Reflector antenna diameter = 1.8m
- F = Focal length of the reflector = 0.48m
- F/D = Focal length / Diameter = 0.267

For this antenna operating in the CW mode, a voltage source at the desired frequency is located at the focus of the parabolic reflector (at the location denoted as "pulser). The applied voltage from the CW source, V^{ant}, is applied to the antenna through a balun, resulting in

differential feed of the transmission line feed arms. As a result, a total applied voltage of $2V$ant is applied across the dish. This source launches a TEM wave on the transmission lines, which reflects from the parabola and propagates as a plane wave to a distant observation point. The radiated fields are defined in a coordinate system (x, y, z), which is a rectangular coordinate system centered on the focal point; x and y are the transverse coordinates; and z is the boresight axis. Further details of this antenna and its operation are available in the literature [2] and in Appendix 1.
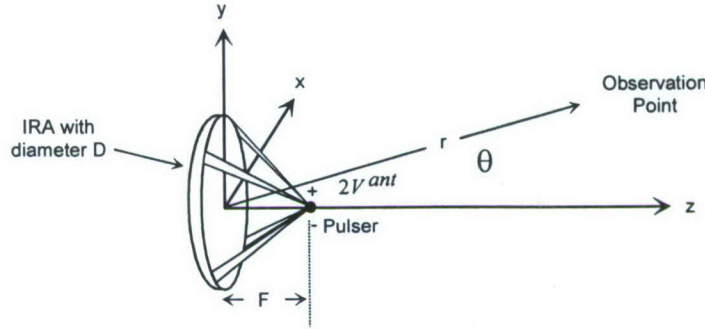
Figure 2. Illustration of the IRA used for CW illumination of the facility in the test program.

Using the analysis developed in [3 and 4], one can calculate the frequency dependent transfer function of the antenna $T_{antenna}$, which is defined as

$$T_{antenna}(\omega, r) = \frac{E(\omega, r)}{V^{ant}(\omega)} \quad (1/m). \tag{1}$$

In this expression, E is the principal component of the radiated E-field from the antenna in the boresight direction (for $\theta = 0$), r is the distance from the antenna, ω is the angular frequency $\omega = 2\pi f$, and $V^{ant}(\omega)$ is the excitation voltage of the antenna at that frequency. Details of this analysis are presented in the references and are not repeated here.

In the measurements discussed here, the antenna was configured to provide a horizontal (with respect to the earth surface) E-field. Figure 3 shows the computed frequency dependent transfer function $T_{antenna}$ for the on-axis radiated E-field produced by the IRA. These data are shown for various ranges from the antenna. It is observed from Figure 3 that in the far-field region, the transfer function is simple proportional to radian frequency, demonstrating that the far radiated field is a derivative of the input voltage.
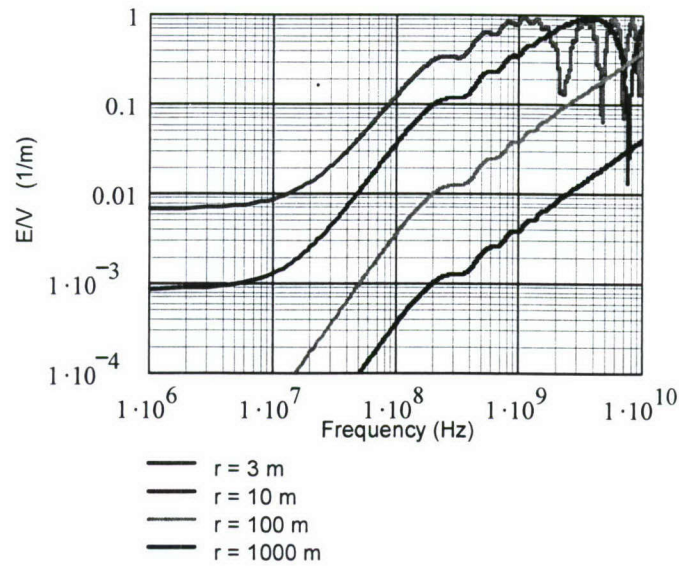
Figure 3. Plots of the frequency dependent transfer function $T_{antenna}$ for the on-axis radiated E-field produced by the IRA, shown for various ranges from the antenna.

In the measurement configuration shown in Figure 1, the estimated range of the IRA source from the facility was on the order of $r \approx 3$ meters, which is shown as the red curve in Figure 3. This curve provides an indication of the incident E-field exciting the facility in the direction of the main beam of the antenna. The data file ***Tantenna.txt*** on the accompanying data file contains the data for the antenna transfer function at 3 meters for a frequency range of 50 to 960 MHz.

Figure 4 shows the H-field probe used to measure the internal field in a specified direction. It is a standard wide-band sensor, which is connected to the recording device (a network analyzer) by a fiber optics cable. This sensor measures only one component of the local H-field, and as a consequence, three separate measurements are required to completely characterize the H-field at an observation point.

The functioning of this type of magnetic field probe is described in ref. [5].
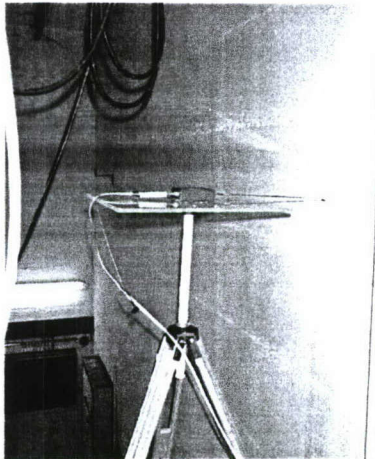
Figure 4. Illustration of the internal H-field probe in the facility.

The measurement of a CW transfer function in the facility is accomplished using the equipment shown in Figure 5.The heart of the measurement system is the computer controlled network analyzer which automatically sweeps through the defined frequency band and extracts the complex ratio of the internal response field divided by the external reference sensor response, which is a transfer function of the facility defined as:

$$T_i^{meas}(\omega) = \frac{H_i^{meas}(\omega)}{V^{ant}(\omega)} .$$

(2)

Here, i denotes the Cartesian component of the H-field being measured, as H_x, H_y or H_z. For the measurements shown here, the external reference signal was chosen to be the *voltage* applied to the radiating IRA. Additional details of this equipment set-up are provided in [1].
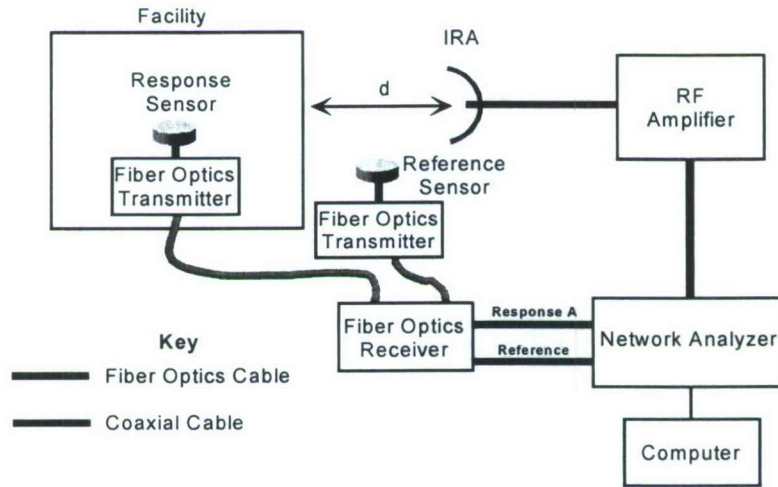
Figure 5. Equipment set-up for the measurement of the CW transfer function within the facility.

3. Typical Measured Data

Figure 6 presents a set of typical H-field transfer functions for the facility, as measured from the experimental set-up of Figure 5. Plotted are the *magnitudes* of the transfer function given in Eq.(2) for the vertical, and two horizontal H-field components. A corresponding *phase* for these transfer functions is also available, but these are not plotted here [1].

Data files for these measured transfer functions over a frequency range from 50 to 960 MHz are provided in the accompanying data file for use in developing a data processing algorithm. These are the files denoted as *Hvert.txt, Hpara.txt* and *Hperp.txt*.
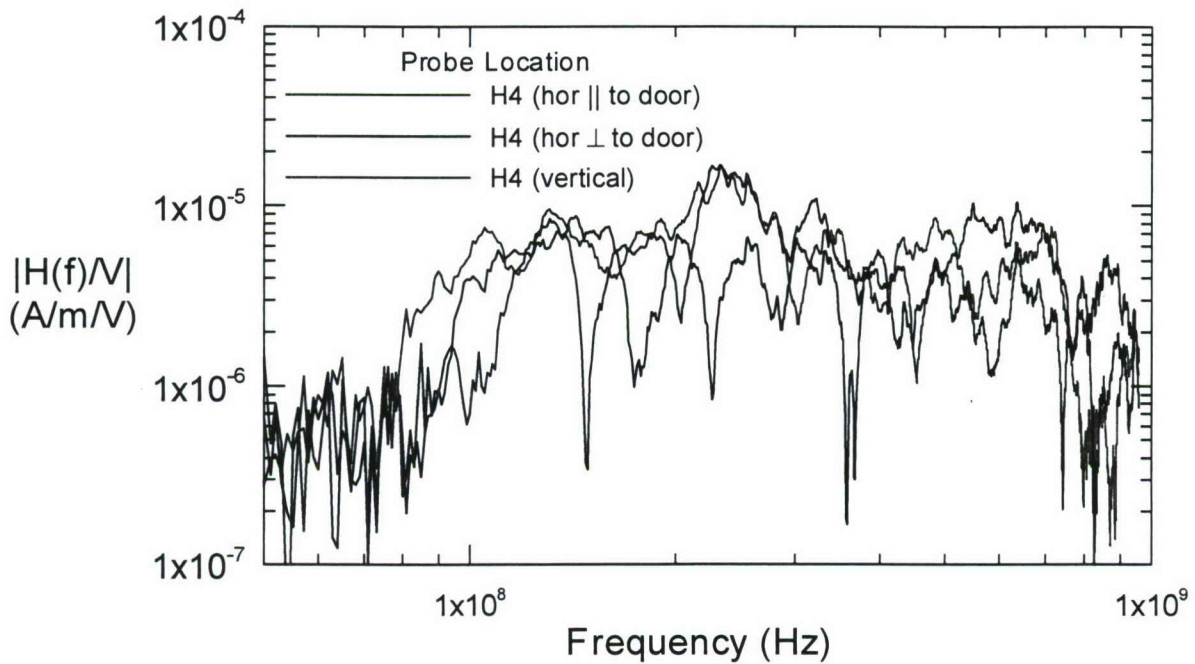
Figure 6. Plots of the measured facility H-field transfer function magnitudes $|T^{meas}(\omega)|=|H_i^{meas}(\omega)/V^{ant}(\omega)|$ for the horizontal H-fields (parallel and perpendicular to a door), as well as the vertical H-field component.

---

[1] Alternatively, one could display the real and imaginary parts of the transfer functions.

4. Use of Measured Data

Frequently in HPEM studies it is required to obtain the transient responses of the internal EM fields and use these to assess the effects on the equipment exposed to these fields. This can be done using the measured EM field transfer functions shown in Figure 6.

4.1 Pulsed Antenna Responses

One transient response is for the IRA source having a pulser attached to its input, as opposed to the CW source that was used for the measurements. This would result in a transient response at the measurement point, and we can estimate this from the CW transfer functions in Figure 6.

For such a transient calculation, we can use a smoothly rising function representing the output of a pulsed voltage source feeding the antenna, as developed by Giri [6]. This analytical expression closely resembles the waveform produced by the High Voltage Pulse Source (HYPS) from Grant Applied Physics [7].

The pertinent parameters of this commercial pulser source are summarized below:

- Peak pulser voltage $\approx$ 3 kV
- 10-90% rise time = nominally 100 ps
- Exponential decay time = nominally 2 ns.

This transient pulser voltage waveform $v(t)$ can be conveniently modeled by the equation

$$
\begin{aligned}
v(t) &= V_o\left(1+a_1\right)e^{-\alpha(t-t_d)/t_d}\frac{\left(1-erf\left(-\sqrt{\pi}\left(t-t_d\right)/t_d\right)\right)}{2} \quad t<t_d \\
&= V_o\left(1+a_1\right)e^{-\alpha(t-t_d)/t_d}\frac{\left(1+erf\left(\sqrt{\pi}\left(t-t_d\right)/t_d\right)\right)}{2} \quad t>t_d
\end{aligned}
\tag{3}
$$

where the following parameters are defined: V_0 = 3000 volts, a_1 = 0.04, α = 0.04 and t_d = 1 ns. The function erf is the error function.

For the waveform in Eq.(3), its spectrum can be determined analytically to be

$$
V(f)=V_o(1+a_1)t_d\frac{e^{(\alpha+j2\pi f t_d)^2/\pi}}{\left(\alpha+j2\pi f t_d\right)}.
\tag{4}
$$

Figure 7 presents plots of this transient pulser waveform and its spectral magnitude.
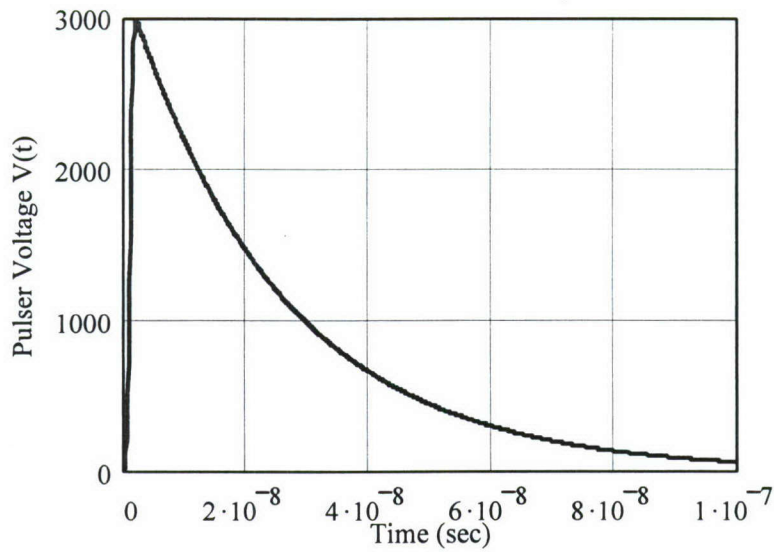
a. Transient pulser waveform
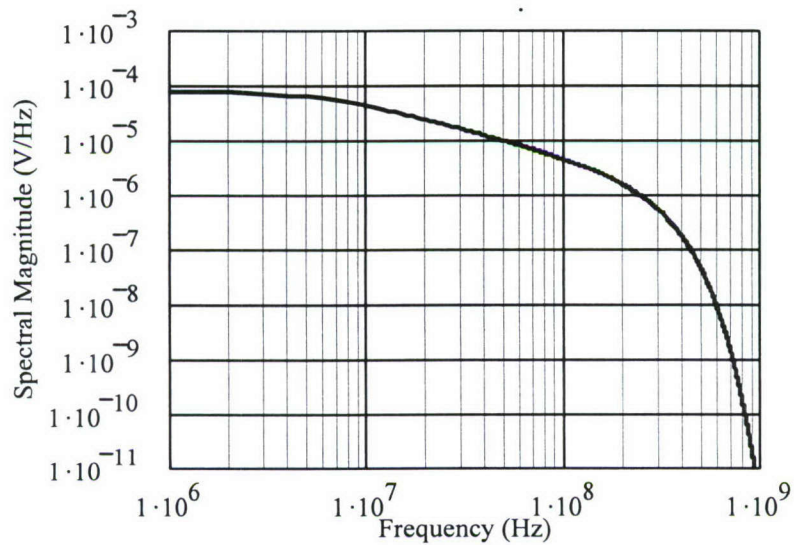
b. Spectral magnitude

Figure 7. Plots of the transient waveform and spectral magnitude of the assumed pulser voltage waveform used to compute transient responses from the measured CW data.

NOTE: The transient near and far fields from the IRA under consideration are documented in Appendix 1of this report.

To compute the transient H-field responses, the measured frequency dependent transfer function of Eq.(2) is multiplied by the excitation spectrum of Eq.(4) to provide the complex H-field spectrum for the pulsed excitation $H^{pulse}(\omega)$ as

$$H^{pulse}(\omega) = T_{meas}(\omega)\, V(\omega). \tag{5}$$

This H-field spectrum is then converted into the time domain using an inverse Fourier transform. Because there may not be 2^N sample points in the measured data, the conventional fast Fourier transform (FFT) cannot be used for this purpose. Instead, a discrete Fourier transform algorithm can be employed to obtain the transient responses.

To illustrate the computed transient responses for the internal H-fields for the pulser excitation, Figure 8 plots these waveforms in a time window from 0 to 1 μs. Note the well-defined time shift in these waveforms, which represents the time delay required for the EM field to penetrate into the facility. Also of interest is the fact that these internal fields ring for 100 – 150 ns, well beyond the time that the excitation pulse is affecting the system. This persistence of the internal response is due to internal resonances within the facility and on facility conductors.
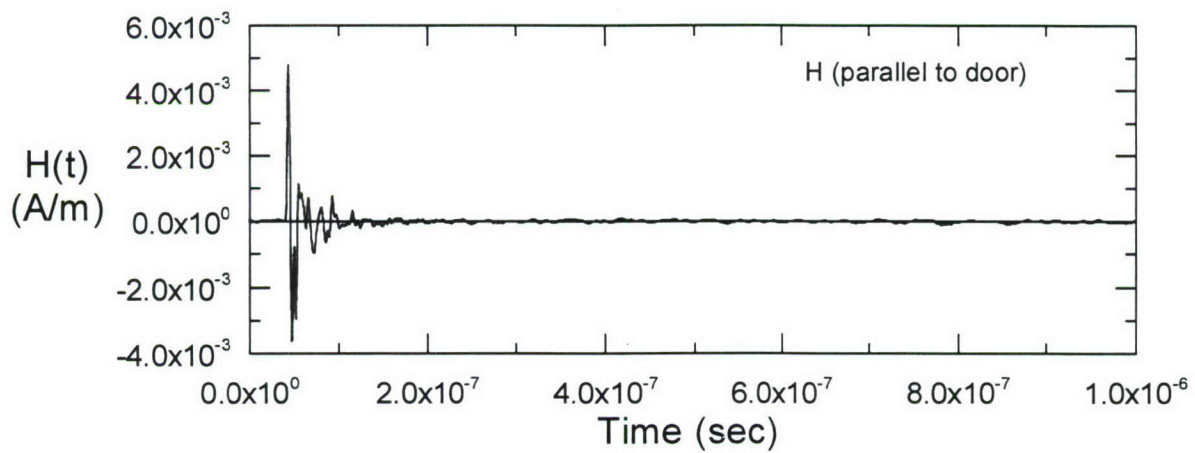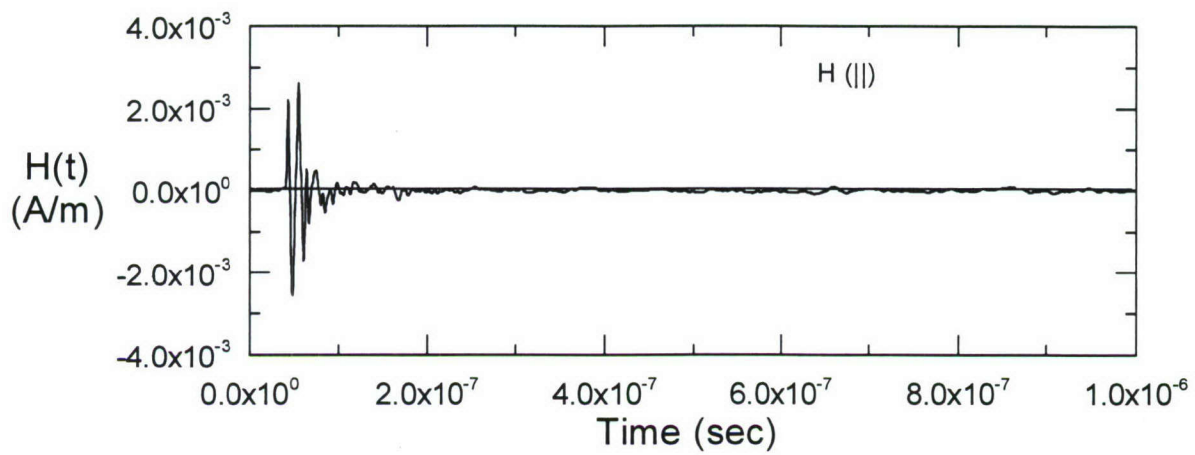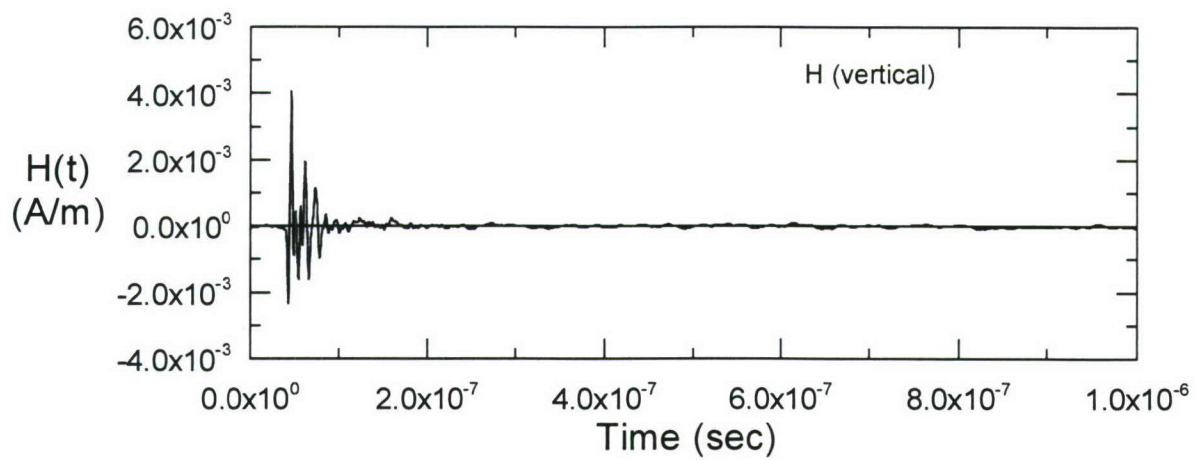
Figure 8. Computed waveforms representing the internal transient H-fields for a pulsed excitation of the IRA antenna.

4.2 Estimation of Plane Wave Responses of the Facility

As noted in Figure 3, the radiated E-field from the IRA depends on the distance between the antenna and the facility. As a result, the internal H-field responses of the facility will depend on the antenna location. With a plane wave excitation of the facility, however, the excitation source is located so far away that the 1/r fall-off of the incident field is not noticeable in the volume occupied by the facility.

To first order, a plane wave response of the facility can be obtained by removing the frequency dependent antenna characteristics in the transfer functions shown in Figure 6. Noting that the measurements of the facility transfer functions were made with the antenna located at a distance of about 3 meters, Eq(1) can be used to eliminate the antenna voltage V^{ant} in Eq.(2) to yield the following relationship between the internal H-fields due to plane wave excitation ($H^{planewave}$) and an incident E-field on the facility:

$$H^{planewave}(\omega) \approx T^{meas}(\omega)\Big|_{r=3m} V^{ant}(\omega)$$

$$\approx \frac{T^{meas}(\omega)\Big|_{r=3m}}{T^{ant}(r,\omega)\Big|_{r=3m}} E^{inc}(\omega) \tag{6}$$

$$\approx T^{planewave}(\omega) E^{inc}(\omega)$$

Thus, knowing the measured H-field transfer function and the antenna radiation transfer function (both obtained for the same distance from the antenna), one can estimate the internal H-fields due to an incident plane wave.

To illustrate transient responses due to an incident plane wave, two different time variations of the incident field are chosen: a Gaussian waveform and a cosine modulated Gaussian waveform. The Gaussian waveform representing the incident E-field on the facility is described by the function

$$E^{inc}(t) = E_o e^{-(2\alpha(t-t_s))^2} \quad \text{(V/m)} \tag{7}$$

with the parameters $t_s = 20$ ns, and $\alpha = 6.0 \times 10^7$ (sec) $^{-1}$.

The cosine modulated Gaussian has the same envelope shape as in Eq.(7), but with a 500 MHz cosinusoidal modulation impressed on the baseboard signal. This waveform is

$$E^{inc}(t) = E_o e^{-(2\alpha(t-t_s))^2} \cos\left(2\pi f_o(t-t_s)\right) \tag{8}$$

with the parameters $t_s = 20$ ns, $\alpha = 6.0 \times 10^7$ (sec) $^{-1}$ and $f_o = 500$ MHz. These two waveforms, together with their respective spectral responses, are shown in Figure 9. For each incident field waveform, the internal H-field responses can be found by multiplying the computed H-field transfer functions of Eq.(6) by the complex spectrum of the excitation waveform to yield the response spectrum. The transient response is then found using an inverse Fourier transform.
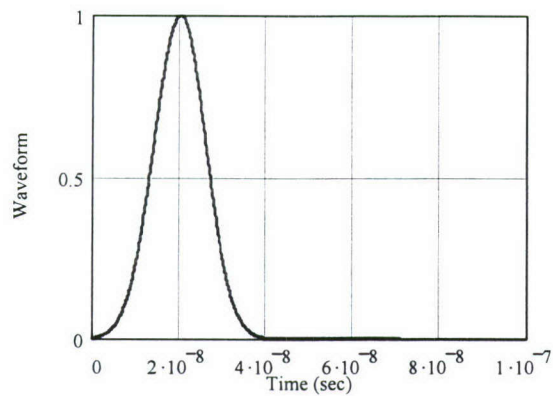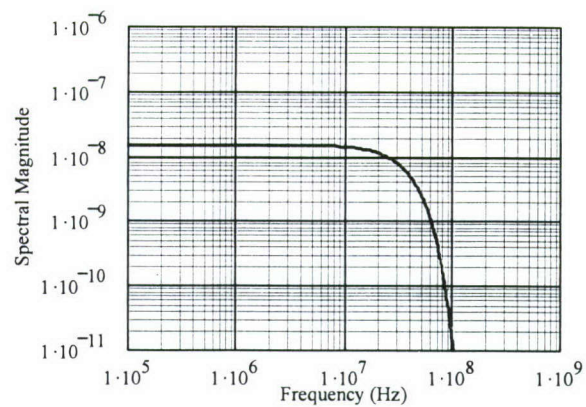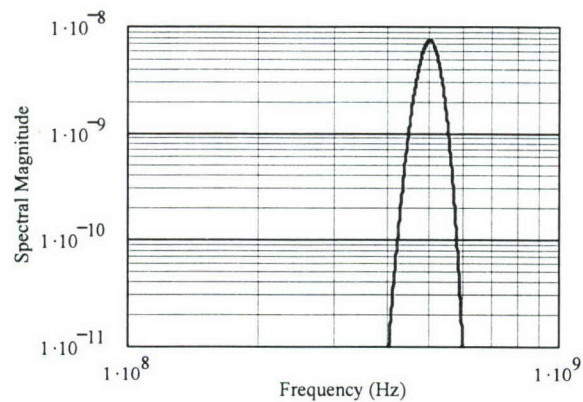
Transient waveform   Spectral magnitude

a. Gaussian excitation waveform.
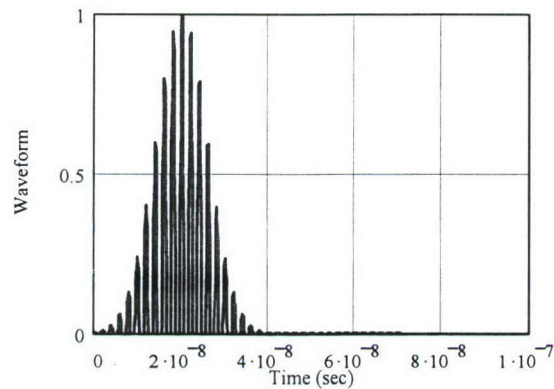
Transient waveform   Spectral magnitude

b. Cosine-modulated Gaussian HPM waveform.

Figure 9. Two excitation waveforms representing the incident HPEM E-field exciting the facility, shown for the amplitude $E_o = 1$ V/m.

5. Suggested Activities

To prepare our UNM team for the acquisition and processing of facility shielding data, there are several tasks that would be useful for the students assisting in the project to consider. These are listed in this section.

5.1 Data Plotting

Figure 6 presents plots of the measured H-field transfer functions (for antenna excitation) as a function of frequency. Develop similar plots for the real and imaginary parts of these transfer functions, as well as plots for the phase functions with ordinate values between $\pm 180^\circ$.

Note that the phase functions "wrap" very rapidly between $\pm 180^\circ$ as the frequency increases. This is due to the time shift of the transient waveform. Noting that a time shift of a waveform by t_1 is equivalent to multiplying the complex spectrum by the term $e^{-j\omega t_1}$, remove the effect of the time shift and again examine the phase. Describe what has happened.

5.2 Fourier Transforms

It is desirable to be able to compute the complex spectrum of a transient waveform $f(t)$, as shown in Figure 7. The inverse Fourier transform is also desired. Keeping in mind that the number of points in the transient record or in the spectrum may not be exactly 2m (as required by the Fast Fourier transform) develop a computer program for performing these transforms. You may assume that the data points all have equal spacing in time and frequency.

With this code developed, check all of the waveform/spectrum plots presented in this note.

5.3 Internal H-field Transient Responses for Antenna Excitation

Using the method outlined in Section 4.1 compute the transient responses for the internal H-fields shown in Figure 8 for the IRA excitation using the pulse excitation Figure 7.

5.4 Internal H-field Transient Responses for Plane Wave Excitation

Using the modified transfer function of Section 4.2 for planewave excitation, compute the internal H-field responses for the two incident E-field waveforms of Figure 9.

5.5 Unit Step Function Response

The unit step function is a common transient waveform that is used for characterizing a system response. This function is defined as $f(t) = U(t-t_1)$ where U is the unit step (Heaviside) function turning on at $t = t_1$. The corresponding Fourier spectrum is know analytically to be

$F(\omega) = e^{-j\omega t_1} / (j\omega)$. Compute the responses for the internal H-fields in the facility due to a step function excitation of the external IRA antenna.

5.6 *IRA Antenna Calculation*

Procure and read reference [4] pertaining to the determination of the on-axis and limited off-axis EM fields from the IRA. Develop a computer program for calculating the on-axis fields. This computer program can be validated by using the results in Appendix-1

6. References

1. IEC INTERNATIONAL STANDARD 61000-4-23, "Electromagnetic compatibility (EMC)–Part 4-23: Testing and measurement techniques – Test methods for protective devices for HEMP and other radiated disturbances", First edition.

2. Giri, D. V., et al., "Design, Fabrication and Testing of a Parabolic Reflector Antenna and Pulser System for Impulse-Like Waveforms", *IEEE Transactions on Plasma Sciences*, Volume 25, No.2., April 1997, pp 318-326.

3. Giri, D. V., and C. E. Baum, "Reflector IRA Design and Boresight Temporal Waveforms", *Sensor and Simulation Notes*, Note 365, 2 February 1994.

4. Mikheev, O. V., et. al, "New Method for Calculating Pulse Radiation from an Antenna With a Reflector", *IEEE Tran. EMC*, Vol 39, No 1, February 1997.

5. See the Prodyn catalog at www.prodyntech.com.

6. Giri, D. V., private conversation, Pro-Tech, Alamo, California.

7. HYPS Pulse Source, S/N 506, Grant Applied Physics, San Francisco, CA.

APPENDIX – 1

Electromagnetic Fields Produced by the IRA System

In this Appendix, we present the calculated electric fields produced by the IRA system. The calculations are based on an analytical approach described in a paper entitled " New method for Calculating Pulse Radiation from an Antenna with a Reflector " by O. V. Mikheev et al., published in *IEEE Transactions on Electromagnetic Compatibility*, Volume 39, number 1, February 1997, pages 48 to 54 [Reference 4 of this report].
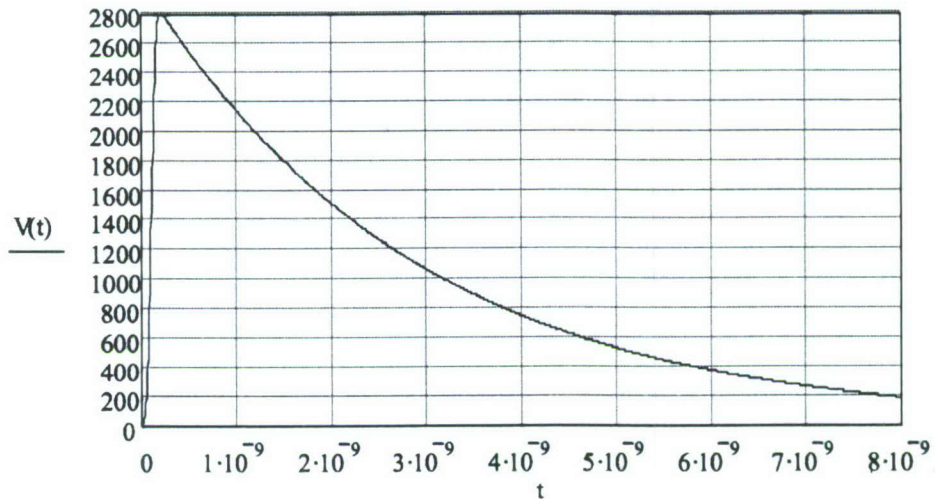
Figure A 1.   Pulser output (peak = 2.8 kV, rise 100ps, FWHM = 2 ns)
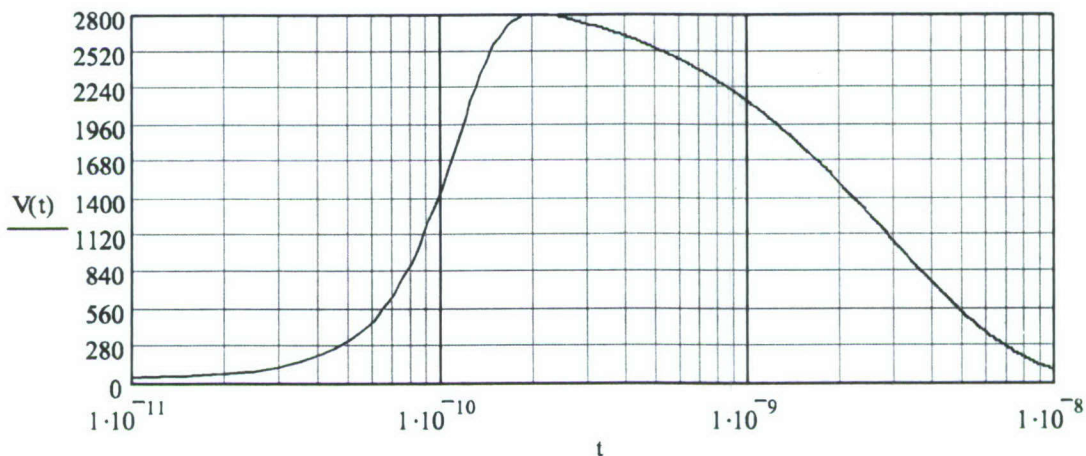
Figure A 2. Rise and decay of pulser voltage, with 10-90% rise time of 100 ps and FWHM = 2 ns
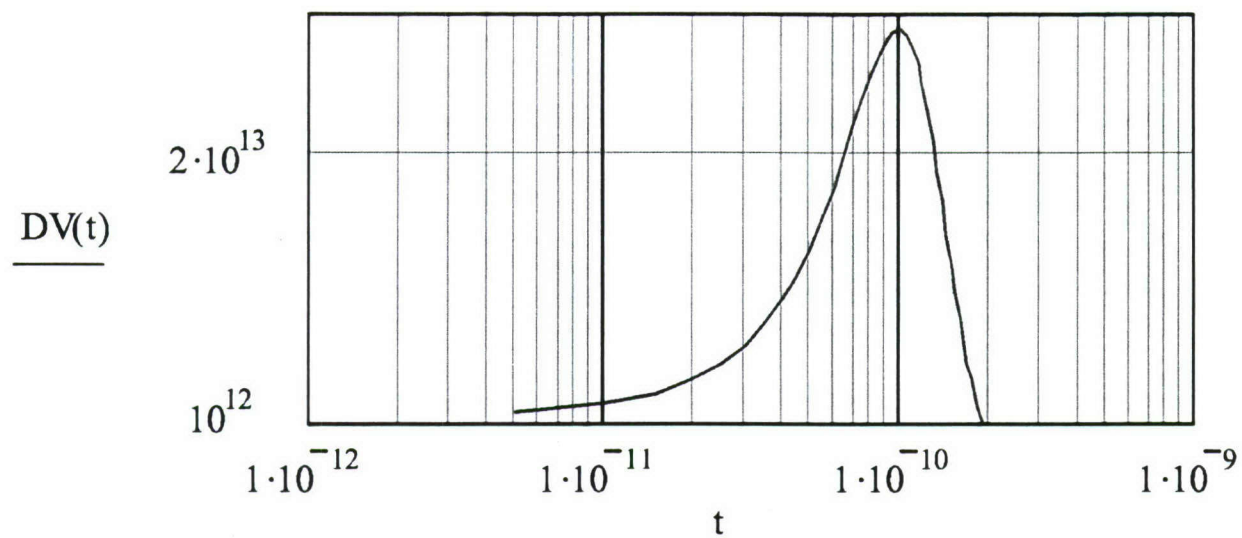
Figure A 3. Derivative of pulser output voltage (peak derivative = 2.875 x 10^{13} V/s).
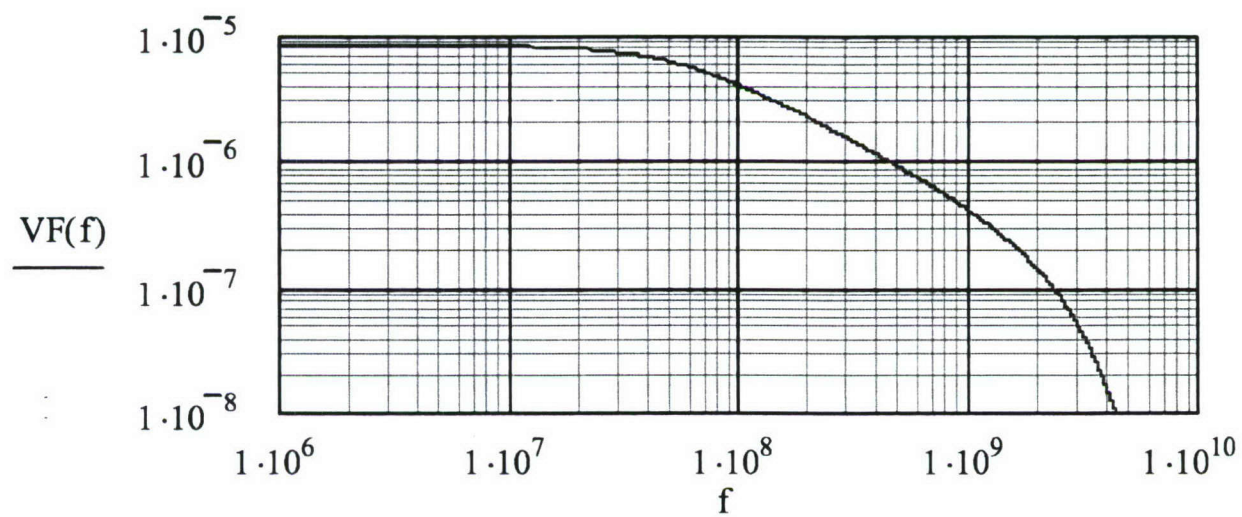
Figure A 4. Spectral magnitude of the pulser voltage

Radiated E-fields for the IRA with 1.8 m (diameter) reflector

The Antenna Geometry:

D = Reflector diameter in meters = 1.8 m
F = Focal length in meters = 0.48 m
F/D = 0.267

The HYPS Pulser Characteristics:

V_0 = Pulser voltage peak = 2,800 Volts
t_{rise} = 10-90% risetime = 100 ps
t_{decay} = exponential decay time = 2 ns

Observation Point: (x,y,z) = coordinates in meters
$\quad\quad\quad\quad\quad\quad\quad\quad$ x and z are the transverse axes
$\quad\quad\quad\quad\quad\quad\quad\quad$ y is the boresight axis.

Computed Fields :

$E(x,y,z,t)$ = E- field in V/m
$M(x,y,z,f)$ = Spectral magnitude of E-field in V/m/Hz
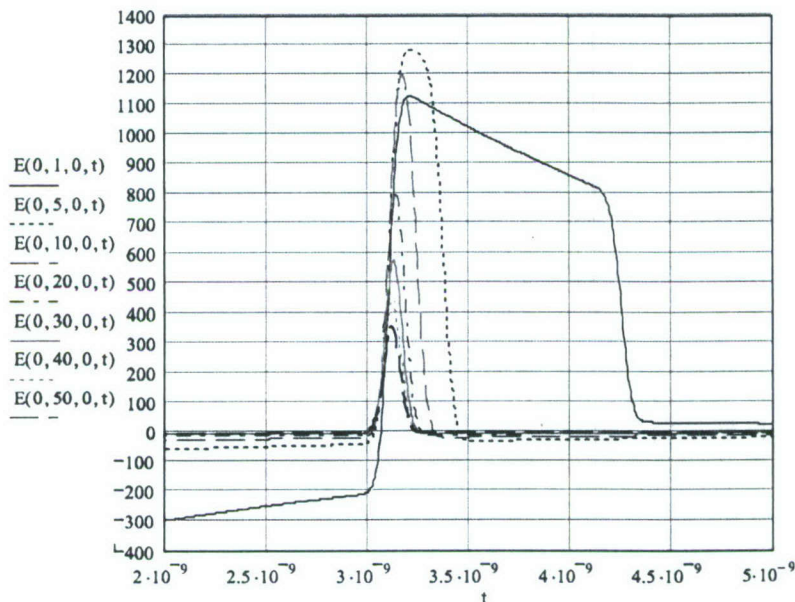
Figure A 5. **Near and Far Field on Bore sight at Various Distances**
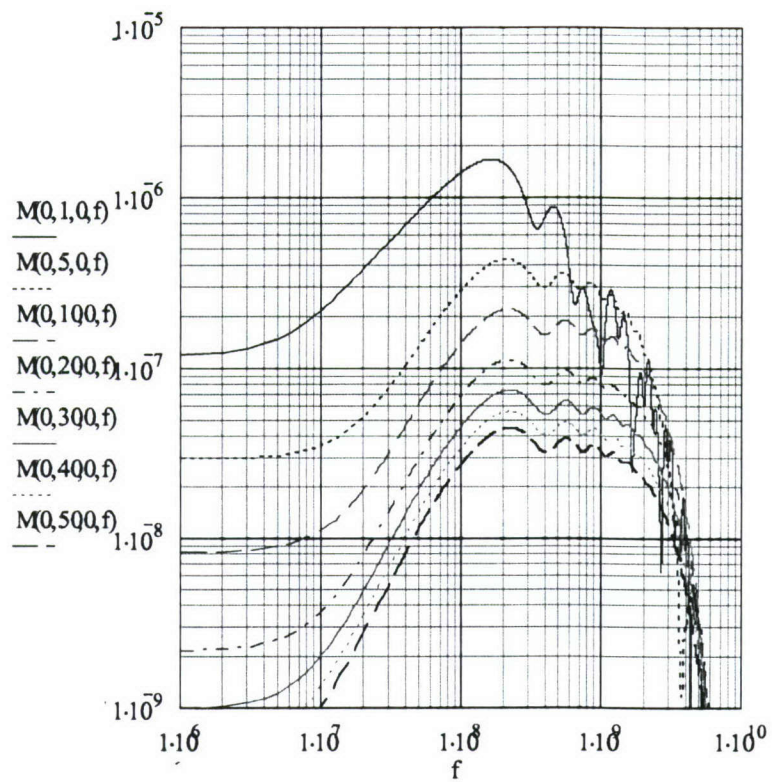
Figure A 6.Spectral Magnitude of the Bore Sight Electric Field at Various Distances
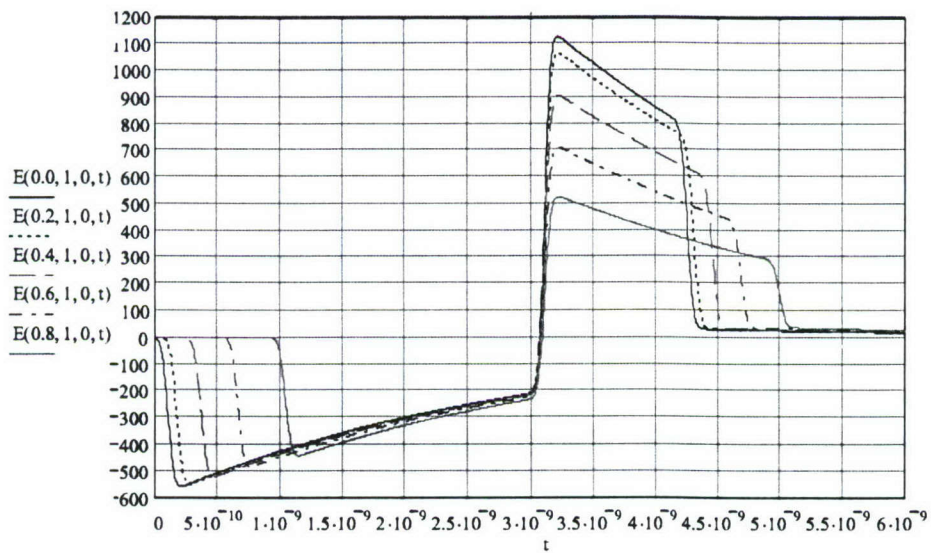
Figure A 7.Temporal electric field at various points along a transverse line, at bore sight distance of 1 m

$M(0.0, 1, 0, f)$ ——
$M(0.2, 1, 0, f)$ ——
$M(0.4, 1, 0, f)$ ‑ ‑ ‑ ‑
$M(0.6, 1, 0, f)$ ‑ ‑
$M(0.8, 1, 0, f)$ — —
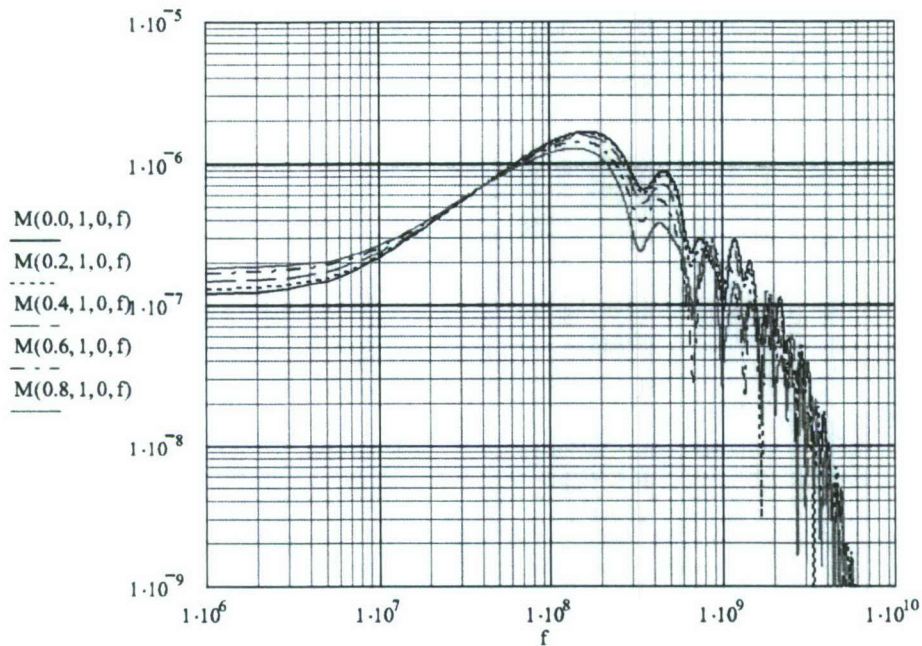
Figure A 8. Spectral magnitude of electric field at various points along a transverse line, at bore sight distance of 1 m, corresponding to the time domain results of Figure A 7.

Comments about the field calculations:

The computational model is restricted to one radius of the reflector along the transverse directions. In other words, we can compute fields (time and frequency) within a cylindrical volume with the reflector as the diameter, and in front of the reflector.

In general, we see the prepulse (negative), impulse (positive) and post pulse (bipolar)

- The prepulse is the direct signal from the source, without the antenna being seen.
- The impulse is the signal off of the reflector.
- The post pulse is the stuff that happens after the impulse.

Observations about the field calculations:

If one moves along a transverse line at a boresight distance of 1m (see Figure A 7), then

1. The prepulse arrives later and later, as it should, since the observer is farther and farther away.

2. The prepulse amplitude drops to some extent, the distances from the source are not that different

3. The impulse at all locations along this transverse line starts at the same instant of time. The reason for this is that when the spherical wave front from the conical transmission line hits the parabolic mirror, it becomes a plane wave, exactly and hence it must arrive at all points in a vertical plane at the same instant of time.

4. As a consequence of 1 and 3 above, the prepulse duration decreases as you move along the transverse line.

5. The impulse amplitude is falling as you move away from the axis, as it should.

6. The post pulse lasts longer as you move away along the transverse line, because the area under the curve is preserved.

7. In other words, if you move along the transverse line, the pulse gets smaller and fatter.

Appendix B – NMSU Shielding Information

Measurements of the Effectiveness of Mitigation Strategies

Bruce Blevins   Oscar Dominguez

Russ Jedlicka   Sebastian Stewart

Coley Burgess   Ian Sturdevant
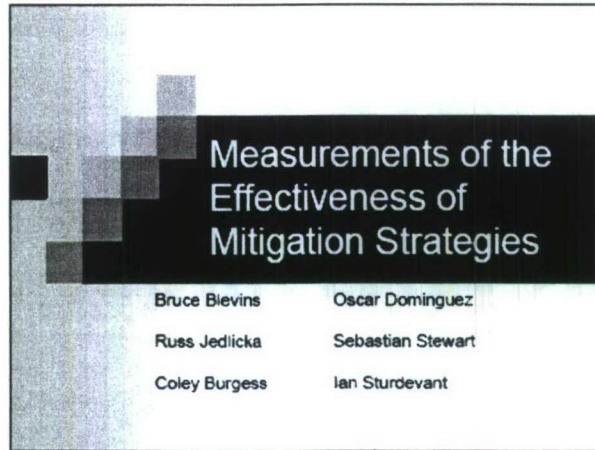
Outline

- Objective
- Equipment Setup
- Aperture Coupling Results
- Measurement Comparisons
- Conductive Coupling Experiment
- Site Measurements
- Conclusions

Objective

Test Shielding Effectiveness of Various Materials over a Band of Frequencies Ranging from 400 MHz to 3 GHz.

Experimental Setup

Receive Antenna Location

Material Under Test

Metallic Frame
(Screws on 1 inch spacing, RF Gasket)
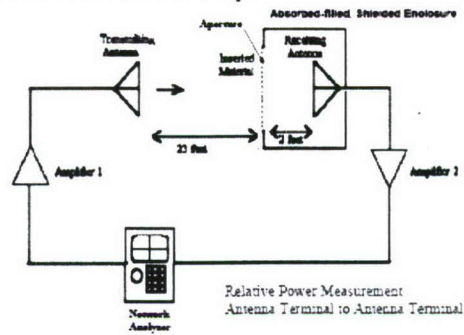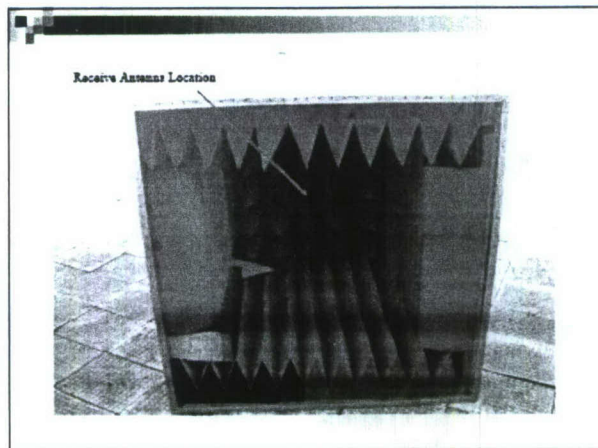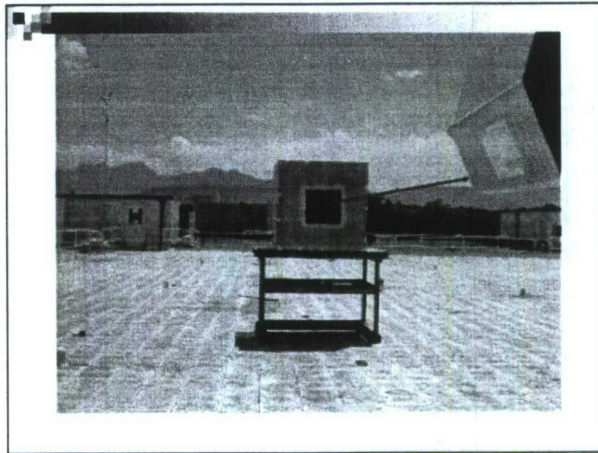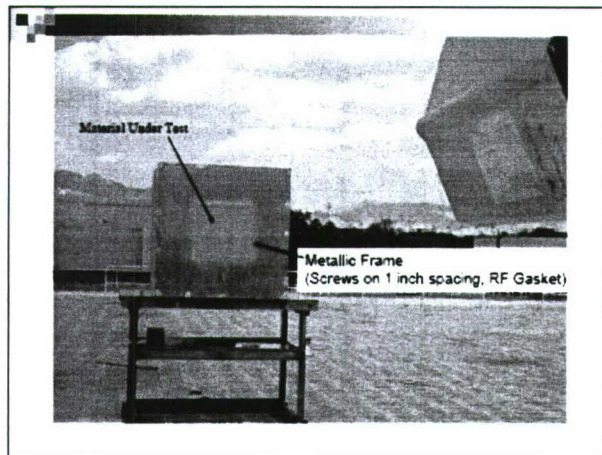
Free Space Measurement

Log Periodic Antenna
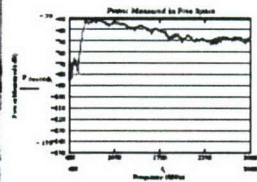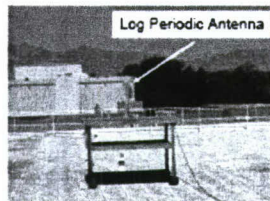
Measurement Relative to Calibration
Cable-to-Cable

Measurement with Box Aperture Open
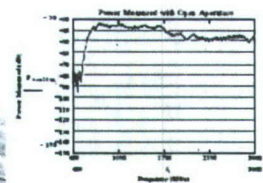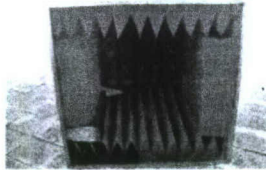
Measurement Relative to Calibration
Cable-to-Cable

Measurement with Gasket in Place
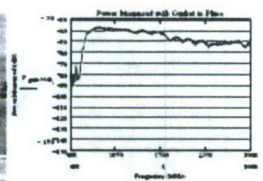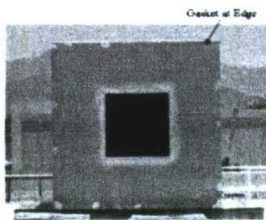
Measurement Relative to Calibration
Cable-to-Cable

Difference w.r.t. free space small enough that measurements that follow will
be compared to the open-aperture case.

Isolation Measurements Using Metal Plate Over Aperture

Measurement Relative to Calibration Cable-to-Cable
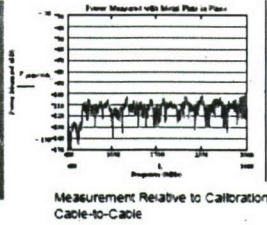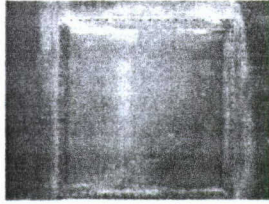
Results: One Inch Wire Mesh Measurements

Measurement Relative to Open Aperture
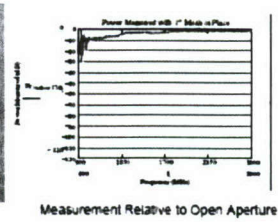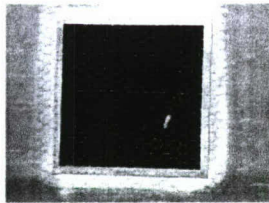
Results: Half Inch Wire Mesh Measurement
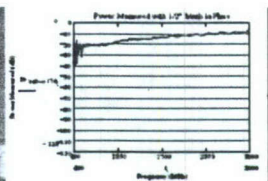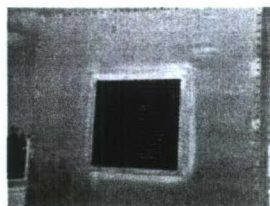
Measurement Relative to Open Aperture
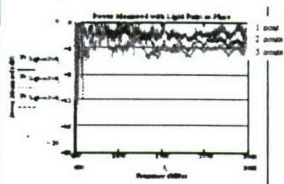

Results: Quarter Inch Wire Mesh Measurements
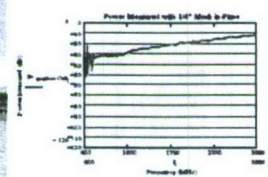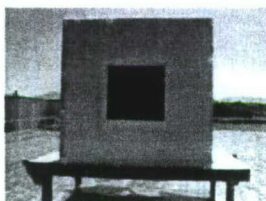
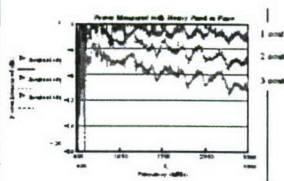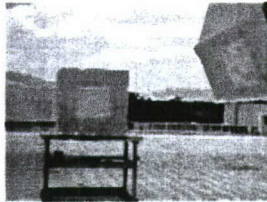Measurement Relative to Open Aperture

Results: Fine Wire Mesh Measurements
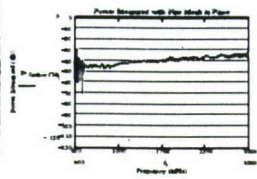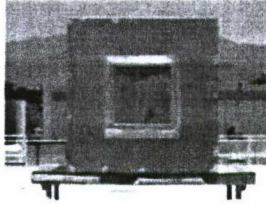
Measurement Relative to Open Aperture

Results: Fabric Measurements
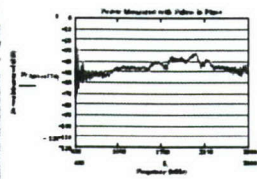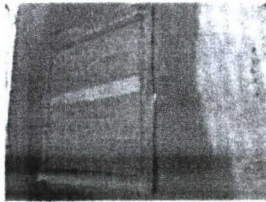
Measurement Relative to Open Aperture

Results: Tint Material (Metalized Mylar) Measurements
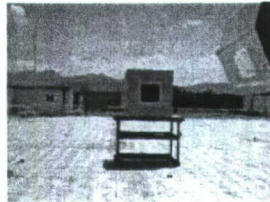
Mylar place on Plexiglas
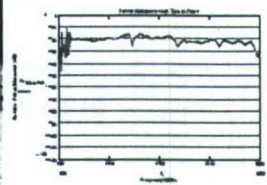
Measurement Relative to Open Aperture

Results: Dry Wall Measurements
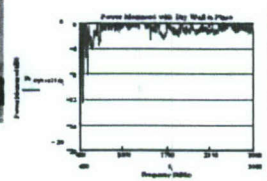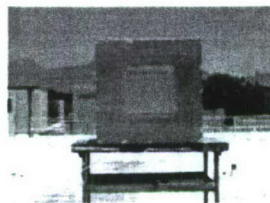
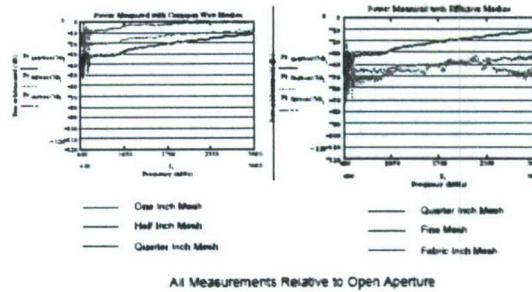Measurement Relative to Open Aperture

Results: Light Paint Coat Measurements
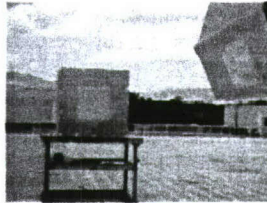
Measurement Relative to Open Aperture

Results: Heavy Paint Coat Measurements

Measurement Relative to Open Aperture

Comparison: Wire Mesh Materials

All Measurements Relative to Open Aperture

Comparison: Expected Wire Mesh Shielding Effectiveness Calculation

$$Z_w = R_w \frac{\sqrt{j\omega\tau_w}\, I_s(\sqrt{j\omega\tau_w})}{2I_1(\sqrt{j\omega\tau_w})}$$

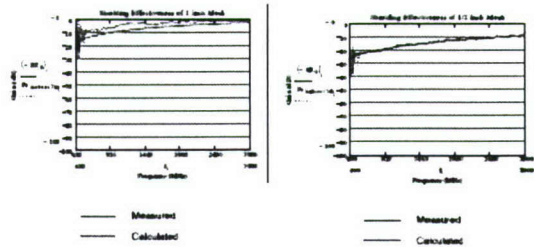$$L_s = \frac{\mu_0 a_s}{2\pi}\ln(1 - e^{-2\pi r_w/d_s})^{-1}$$

$$Z_{s1} = Z_w a_s + j\omega L_s = Z_s$$

$$Z_{s2} = Z_s + \frac{j\omega L_s}{2}\sin(\theta)$$

$$T_1 = \frac{2(Z_{s1}/Z_0)\cos(\theta)}{1 + 2(Z_{s1}/Z_0)\cos(\theta)}$$
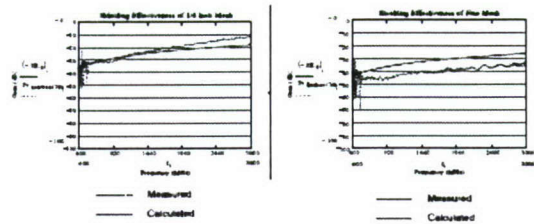
$$T_2 = \frac{2Z_{s2}/Z_0}{2Z_{s2}/Z_0 + \cos(\theta)}$$

$$SE_q(\theta) = -10\log_{10}\left(\frac{1}{2}|T_1(\theta)|^2 + \frac{1}{2}|T_2(\theta)|^2\right)$$

- K. F. Casey, "Electromagnetic Shielding Behavior of Wire-Mesh Screens," IEEE Trans. Electormagn. Compat., vol. EMC-30, pp298-306, Aug. 1988.
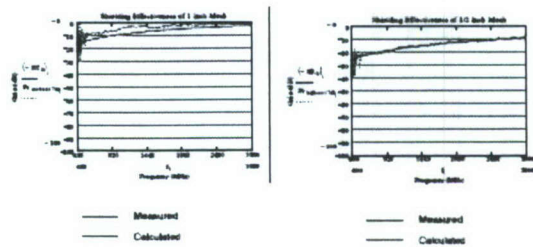
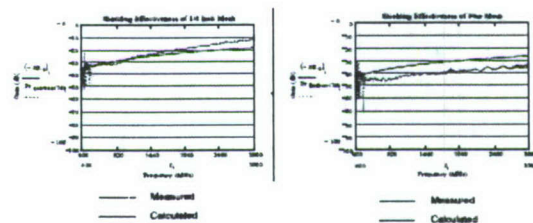# Comparison: Wire Meshes with Predicted Values

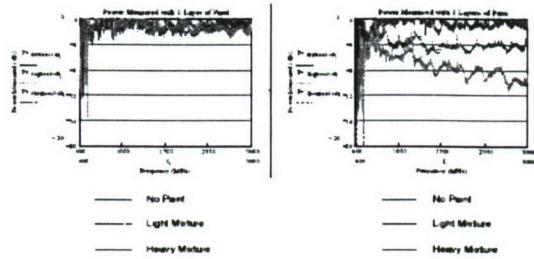# Comparison: Wire Meshes with Predicted Values (Continued)

Comparison: Wire Meshes with Predicted Values

Measured
Calculated

Comparison: Wire Meshes with Predicted Values (Continued)

Measured
Calculated

Comparison: Dry Wall and Paint Layering

| No Paint |
| Light Mixture |
| Heavy Mixture |

| No Paint |
| Light Mixture |
| Heavy Mixture |

Conductive Coupling Experiment

- Plate modified so that external wires can penetrate the shielded enclosure
- Low Q structure and lack of dynamic range produced marginal results.
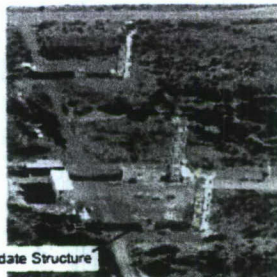- Setup needs to be reconfigured
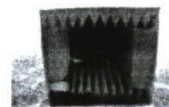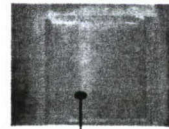
Site Measurements

- Active illumination of a small building within the antenna range complex

- Aperture penetration as well as diffusive coupling through non-metallic walls expected

- Buildings within complex interconnected with RF cables and wiring – controlled conductive experiments can also be run
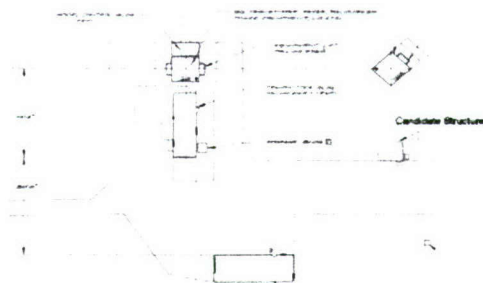
Site Measurements

- Access to site is limited and controlled

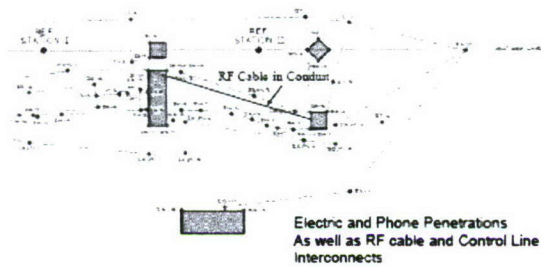- Building size small to moderate

- Building/site can be reconfigured

Candidate Structure

Site Building Layout

Site Building Interconnectivity

Electric and Phone Penetrations
As well as RF cable and Control Line
Interconnects

RF Cable in Conduit

Test Structure North Side

Wire Mesh is Removable
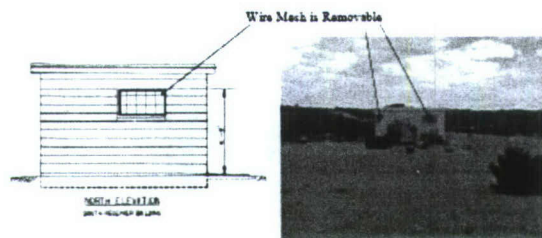
Test Structure East & South Side
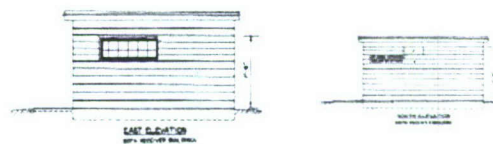
Test Structure West Side
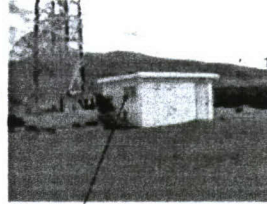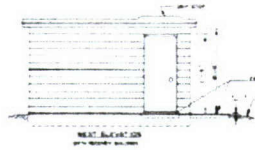
Mesh-covered Window

Test Structure Interior
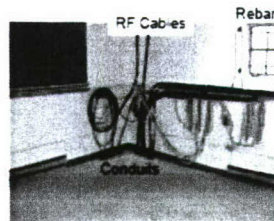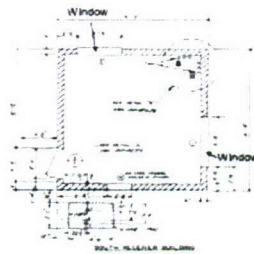
Material Composition of Target Structure
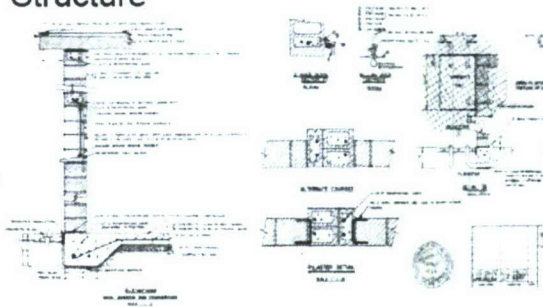
Conclusions

- The RF paint used was ineffective at shielding even when heavily layered. It offers very little shielding in the band investigated.
- The wire meshes performed as expected, and are much better shielding materials than the RF paint.

Conclusions (Continued)

- The fine wire mesh and RF shielding cloth both had relatively high shielding effectiveness (at least for non-hardened configurations).
- The tint, which only offers modest levels of shielding, is more aesthetically appealing than the other methods.

DEPARTMENT OF DEFENSE

DEFENSE TECHNICAL INFORMATION
CENTER
8725 JOHN J. KINGMAN ROAD, SUITE 0944
FORT BELVOIR, VA 22060-6218
2 CYS ATTN: DTIC

DEFENSE THREAT REDUCTION AGENCY
(DTRA)
8725 JOHN J. KINGMAN ROAD, STOP 6201
FT. BELVOIR, VA 22060-6201
ATTN: NTE/T. HANN
ATTN: NTES/M. ROONEY
ATTN: NTES/R. DAVIS

DEFENSE THREAT REDUCTION AGENCY
(DTRA)
ALBUQUERQUE OPERATIONS
1680 TEXAS STREET, SE
KIRTLAND AFB, NM 87117-5669
ATTN: CXT/J. THOMAS

DEFENSE THREAT REDUCTION AGENCY
(DTRA)
1680 TEXAS STREET, SE
KIRTLAND AFB, NM 87117-5669
2 CYS ATTN: DTRIAC

DEPARTMENT OF THE ARMY

US ARMY NUCLEAR AND CHEMICAL
AGENCY
7150 HEELER LOOP, SUITE 101
SPRINGFIELD, VA 22150-3164
ATTN: R. PFEFFER

ARMY RESEARCH LABORATORIES
2800 POWDER MILL ROAD
ADELPHI, MD 20783-1197
ATTN: AMSRL-SE-DD/E. SHAFFER
ATTN: AMSRL-SE-DE/J. TATUM

ARMY TEST AND EVALUATION COMMAND
4501 FORD AVENUE
ALEXANDRIA, VA 22302
ATTN: TECHNICAL DIRECTOR/B. BARR

DEPARTMENT OF THE NAVY

NAVAL RESEARCH LABORATORY
4555 OVERLOOK AVENUE, SE
WASHINGTON, DC 20375-5000
ATTN: CODE 5712/CAROL SULLIVAN
ATTN: CODE 5745/T. ANDREADIS

ATTN: CODE 5745/M. RADER

NAVAL SURFACE WARFARE CENTER
DAHLGREN DIVISION
11720 DAHLGREN ROAD
DAHLGREN, VA 22448-5100
ATTN: D. STOUT
ATTN: S. GRIFFITH
ATTN: F. PETERKIN

NAVAL SURFACE WARFARE CENTER
DAHLGREN DIVISION
BUILDING 1470/ROOM 1405
DAHLGREN DIVISION
DAHLGREN, VA 22448-5100
ATTN: CODE B20/V. DEPRENGER

NAVAL SEA SYSTEMS COMMAND
BUILDING 197, ROOM 2W2912
1333 ISAAC HULL AVENUE, SE
WASHINGTON NAVY YARD
WASHINGTON, D.C. 20376-5100
ATTN: CODE PMS-405T/G. NOLTING

OFFICE OF NAVAL RESEARCH
875 NORTH RANDOLPH STREET
SUITE 1425
ARLINGTON, VA 22203-1995
ATTN: CODE 312/P. GROUNDS

DEPARTMENT OF THE AIR FORCE

AIR FORCE OFFICE OF SCIENTIFIC
RESEARCH (AFOSR)
875 NORTH RANDOLPH STREET
ARLINGTON, VA 22203
ATTN: AFOSR/NE/MAJ. R. UMSTATTD

AIR FORCE OPERATIONAL TEST AND
EVALUATION CENTER
8500 GIBSON BOULEVARD, SE
ALBUQUERQUE, NM 87117
ATTN: AFOTEC CN/M. WILLIAMS

AIR FORCE RESEARCH LABORATORY
3550 ABERDEEN AVENUE, SE
KIRTLAND AFB, NM 87117-5776
ATTN: DE/W. BAKER
ATTN: DEH/R. PETERKIN, JR.
ATTN: DEH/T. HUSSEY
ATTN: DEH/P. TURCHI
ATTN: DEHA/D. DEVANY
ATTN: DEHE/D. SCHAFER
ATTN: DEHE/T. CLARKE
ATTN: DEH/M. HARRISON

ATTN: DEHP/W. PRATHER

DEPARTMENT OF ENERGY

SANDIA NATIONAL LABORATORIES
ATTN: MAIL SERVICES
P.O. BOX 5800
ALBUQUERQUE, NM 87185-0459
ATTN: D. FORDHAM
ATTN: MALCOLM BUTTRAM
ATTN: COLLINS CLARKE

**DEPARTMENT OF DEFENSE
CONTRACTORS**

ATK MISSION RESEARCH
8560 CINDERBED ROAD, SUITE 700
NEWINGTON, VA 22122
ATTN: J. PASOUR
ATTN: J. MCADOO

ATK MISSION RESEARCH
P.O. DRAWER 719
SANTA BARBARA, CA 93102
ATTN: F. GUIGLIANO
ATTN: R. GOLDFLAM

MICROWAVE SCIENCES, INC.
1041 LOS ARABIS LANE
LAFAYETTE, CA 94549
ATTN: J. BENFORD

FISCHER CUSTOM COMMUNICATIONS
7920 ARJONS, SUITE C
SAN DIEGO, CA 92128
ATTN: R. STEWART

ITT INDUSTRIES
ITT SYSTEMS CORPORATION
1680 TEXAS STREET, SE
KIRTLAND AFB, NM 87117-5669
ATTN: AO DTRIAC
ATTN: DTRIAC/DARE

L-3 TITAN/JAYCOR CORPORATION
5575 TECH CENTER DRIVE
SUITE 310
COLORADO SPRINGS, CO 80919
ATTN: M. BELL
ATTN: D. FROMME

L-3 TITAN CORPORATION
3394 CARMEL MOUNTAIN ROAD
SAN DIEGO, CA 92121
ATTN: P. COAKLEY
ATTN: D. WALTERS
ATTN: D. BREUNER

L-3 TITAN JAYCOR
3700 STATE STREET, SUITE 300
SANTA BARBARA, CA 93105
ATTN: W. CREVIER
ATTN: J. MORROW-JONES

NORTHROP GRUMMAN
222 W. SIXTH STREET, 5TH FLOOR
SAN PEDRO, CA 90731-0471
ATTN: C. MO

PRO-TECH
11-C ORCHARD COURT
ALAMO, CA 94507-1541
ATTN: D. GIRI

DR. FRED TESCHE
EM CONSULTANT
1519 MILLER MOUNTAIN ROAD
SALUDA, NC 28773
ATTN: F. TESCHE

UNIVERSITY OF MARYLAND
INSTITUTE FOR RESEARCH IN
ELECTRONICS AND APPLIED PHYSICS
ENERGY RESEARCH FACILITY (BLDG. #223)
PAINT BRANCH DRIVE
COLLEGE PARK, MD 20742-3511
ATTN: V. GRANATSTEIN
ATTN: S. HEMMADY

OVPRED
SCHOLES HALL STE 327
1 UNIVERSITY OF NEW MEXICO
ALBUQUERQUE, NM 87131-0001
ATTN: C. CHRISTODOULOU
ATTN: J. GAUDET
ATTN: F. GILFEATHER
5 CYS ATTN: E. SCHAMILOGLU